Journal of Solid State Chemistry **151,** 190–209 (2000)
doi:10.1006/jssc.1999.8640, available online at http://www.idealibrary.com on IDEAL®

Evolution of Oxygen-Vacancy Ordered Crystal Structures in the Perovskite Series $Sr_nFe_nO_{3n-1}$ ($n = 2$, 4, 8, and ∞), and the Relationship to Electronic and Magnetic Properties[1]

J. P. Hodges,[2] S. Short, and J. D. Jorgensen

Materials Science Division, Argonne National Laboratory, Argonne, Illinois 60439

and

X. Xiong, B. Dabrowski, S. M. Mini, and C. W. Kimball

Department of Physics, Northern Illinois University, De Kalb, Illinois 60115

Received

Over the oxygen composition range $2.5 \leq x \leq 3.0$, the $SrFeO_x$ system exists as four distinct compounds with the nominal composition $Sr_nFe_nO_{3n-1}$ ($n = 2$, 4, 8, and ∞). The end member $SrFeO_3$ ($n = \infty$) possesses a simple cubic perovskite crystal structure, whereas the oxygen-deficient ($n = 2$, 4, and 8) members each adopt a different vacancy-ordered perovskite crystal structure. Using time-of-flight neutron powder diffraction, we show that previously proposed structures for the $Sr_4Fe_4O_{11}$ ($n = 4$) and $Sr_8Fe_8O_{23}$ ($n = 8$) compounds are incorrect. We determine the correct crystal structures for $Sr_4Fe_4O_{11}$ (orthorhombic, space group *Cmmm*, $a = 10.974(1)$ Å, $b = 7.702(1)$ Å, and $c = 5.473(1)$ Å) and $Sr_8Fe_8O_{23}$ (tetragonal, space group *I4/mmm*, $a = 10.929(1)$ Å and $c = 7.698(1)$ Å) through comparisons of the goodness of fit for Rietveld refinements of candidate models and bond-length distributions for each model. Using the correct crystal structures, we are able to assign valence states to the Fe crystallographic sites and to achieve consistency with published Mössbauer results for the same compounds. © 2000 Academic Press

INTRODUCTION

The variable-valence $SrFeO_x$ ($2.5 \leq x \leq 3.0$) perovskite system is an instructive model for study of the effects of oxygen-vacancy ordering on crystal structure and electronic properties. The oxygen-deficient end member, $SrFeO_{2.5}$, is an orthorhombic oxygen-vacancy-ordered perovskite of brownmillerite structure type (1). In this compound the Fe^{3+} cations are well behaved in the ionic regime, and as such the compound is an antiferromagnetic Mott-type insulator. The other end member, cubic perovskite $SrFeO_3$, exhibits the coexistence of metallic conductivity ($\sigma \approx 10^3\ S\,cm^{-1}$) (2, 3) and screw-type antiferromagnetic ordering ($T_N \approx 130$ K) (4). This unusual combination of metallic conductivity and antiferromagnetism in $SrFeO_3$ is related to the high valence of the formally Fe^{4+} cations by way of the enhanced Fe–O covalency and $O{:}2p \rightarrow Fe{:}3d$ charge transfer (5–7). From the low-temperature magnetic flux densities measured by Mössbauer spectroscopy, high-spin electronic configurations have been determined for the $Fe^{4+}{:}d^4$ and $Fe^{3+}{:}d^5$ cations present in the series end members $SrFeO_3$ and $SrFeO_{2.5}$, respectively (1, 8).

Initial studies of the $SrFeO_x$ system as a function of oxygen content revealed the existence of possibly one or more intermediate oxygen-vacancy-ordered $SrFeO_x$ phases; however, important discrepancies exist between the individual studies (1, 2, 9, 10). These problems can largely be attributed to the use of differing synthesis conditions and the associated difficulties of X-ray powder diffraction on near-cubic perovskites. Subsequent investigations (11–13) resolved many of the early discrepancies concerning the nonstoichiometric chemistry of $SrFeO_x$. The pertinent results of these studies can be outlined as follows. Above a composition-dependent transition temperature $T_t(x)$, $SrFeO_x$ forms a continuous oxygen-vacancy-disordered solid–solution with the cubic perovskite structure. On cooling, three miscibility gaps arise which divide the $SrFeO_x$ system into four structurally distinct phases. The existence of the two intermediate vacancy-ordered perovskite phases was confirmed by a combination of electron diffraction and

---

[1] The U.S. Government's right to retain a nonexclusive royalty-free license in and to the copyright covering this paper, for governmental purposes, is acknowledged.

[2] To whom correspondence should be addressed. E-mail: hodges@anl.gov.

0022-4596/00 $35.00

high-resolution X-ray powder diffraction techniques (12). These two phases of nominal compositions $SrFeO_{2.75}$ and $SrFeO_{2.875}$ were reported to have orthorhombic $2\sqrt{2}a_p \times 2a_p \times \sqrt{2}a_p$ and tetragonal $2\sqrt{2}a_p \times 2\sqrt{2}a_p \times 2a_p$ supercells, respectively (where a_p denotes the unit-cell edge of the perovskite subcell). Since these phases are formed within relatively narrow compositional ranges, they can be considered as members of the ideal series $Sr_nFe_nO_{3n-1}$, where $n = \infty$, 8, 4, and 2.

In this paper we report the results of a neutron powder diffraction study of the four phases of $Sr_nFe_nO_{3n-1}$ ($n = 2, 4$, 8 and ∞). Through comparison of Rietveld refinements of appropriate candidate oxygen-vacancy-ordered perovskite models for the $Sr_4Fe_4O_{11}$ ($n = 4$) and $Sr_8Fe_8O_{23}$ ($n = 8$) phases, we determine the correct crystal structures and show that all previously reported structures are incorrect. Using the correct structures, we are able to assign valence states to the Fe crystallographic sites and to achieve consistency with published Mössbauer results for the same compounds. The relationship between crystal structure and some of the interesting electronic and magnetic properties of these phases is then discussed.

SYNTHESIS AND NEUTRON POWDER DIFFRACTION

A 2.5-g sample of $SrFeO_x$ was prepared from spectroscopic-grade $SrCO_3$ and 90% ^{57}Fe isotopically enriched Fe_2O_3 (the ^{57}Fe isotope was used because the same samples were used in a study of the phonon density of states by inelastic nuclear resonant X-ray scattering (14)). Stoichiometric amounts of $SrCO_3$ and Fe_2O_3 were ground together, pressed into a pellet, and fired at 1250°C for 24 hr followed by slow cooling to room temperature. An oxygen content of $x = 2.870(5)$ was determined for the as-synthesized sample of $SrFeO_x$ by thermogravimetric analysis (TGA). The $SrFeO_x$ sample was then annealed at 400°C under 30 MPa of pure oxygen for 24 hr and slowly cooled to 200°C at 1°C/hr. TGA revealed that this high-pressure oxygen annealing step had increased the oxygen content of $SrFeO_x$ to $x = 2.998(5)$. This $SrFeO_3$ sample was then separated into four smaller samples of approximately 600 mg each. The oxygen contents of three samples were then individually adjusted to desired values directly on the TGA balance by annealing in appropriate flowing atmospheres. An $SrFeO_{2.5}$ brownmillerite phase was obtained by heating $SrFeO_3$ in a 5% H_2/Ar gas mixture at 500°C for 12 hr. An $SrFeO_x$ sample with $x = 2.740(5)$ was obtained by heating $SrFeO_3$ to 850°C in a 200 ppm O_2/Ar gas mixture, slowly cooling to 550°C, and then rapidly cooling to room temperature. An $SrFeO_x$ sample with $x = 2.860(5)$ was obtained by heating $SrFeO_3$ to 850°C in a 12% O_2/Ar gas mixture, slowly cooling to 400°C, and then rapidly cooling to room temperature.

Time-of-flight neutron powder diffraction spectra were collected from the four $SrFeO_x$ ($x = 3.0$, 2.86, 2.74, and 2.50) samples using the Special Environment Powder Diffractometer at Argonne's Intense Pulsed Neutron Source (15). Diffraction data were collected on all detector banks. However, only the analysis of the high-resolution back-scattering data ($\Delta d/d = 0.035$) is presented here. Model crystal structures were refined by the Rietveld method (16) using the GSAS suite of programs (17). The magnetic form factor used for Fe^{3+} cations was taken from the *International Tables for Crystallography* (18).

OXYGEN-VACANCY ORDERING SCHEMES IN $Sr_nFe_nO_{3n-1}$ ($n = 2$, 4, AND 8)

The oxygen-deficient end-member phase $Sr_2Fe_2O_5$ ($n = 2$) possesses a brownmillerite-type crystal structure (1). The brownmillerite structure type is a classic example of an oxygen-vacancy-ordered perovskite. It is derived from the parent cubic ABO_3 perovskite structure by creating lines of oxygen vacancies along the $[101]_p$ direction in every other $(010)_p$ plane, producing a $\sqrt{2}a_p \times 4a_p \times \sqrt{2}a_p$ supercell. A schematic representation of the oxygen-vacancy ordering scheme of brownmillerite is shown in Fig. 1a. Following relaxation, the resulting structure contains alternating layers of BO_6 octahedra (O) and BO_4 tetrahedra (T and T') perpendicular to the y-axis. A polyhedral representation of a brownmillerite $A_2B_2O_5$ unit cell is shown in Fig. 2a. Subtle structural differences, arising from the variety of atomic relaxation displacements possible, exist between various brownmillerite $A_2B_2O_5$ compounds. In $Ca_2Fe_2O_5$ and Ca_2FeAlO_5 (19, 20), the zig-zag relationship between adjacent FeO_4 chains within any individual FeO_4 layer is essentially identical. However, the symmetry relations between T and T' layers are $\bar{1}$ and 2, resulting in the adoption of *Pcmn* and *Ibm*2 space groups, respectively. To illustrate the interchain relationship for the Ca_2FeAlO_5 case, a brownmillerite unit cell of *Ibm*2 crystal symmetry and associated expanded views of the $y = 0.25$ and 0.75 FeO_4 layers are shown in Figs. 2a and 2b. The essential structural difference between $Ca_2Fe_2O_5$ and Ca_2FeAlO_5 corresponds to replacing the T' layer in Fig. 2b with its xy mirror image. In contrast to these fully ordered brownmillerite compounds, a neutron powder and electron diffraction study of $Sr_2Fe_2O_5$ indicated a degree of structural disorder (21). This disorder was interpreted as arising from an irregular occurrence of a $\bar{1}$, rather than a 2, symmetry relationship between adjacent FeO_4 layers. The crystal structure was, therefore, refined in the higher symmetry *Icmm* space group. A subsequent single-crystal X-ray diffraction study of $Sr_2Fe_2O_5$, however, determined a fully ordered structure consistent with the *Ibm*2 space group (22). The results of neutron powder diffraction studies of the closely related brownmillerite compounds Sr_2CoFeO_5 and $Sr_2Co_2O_5$ are consistent

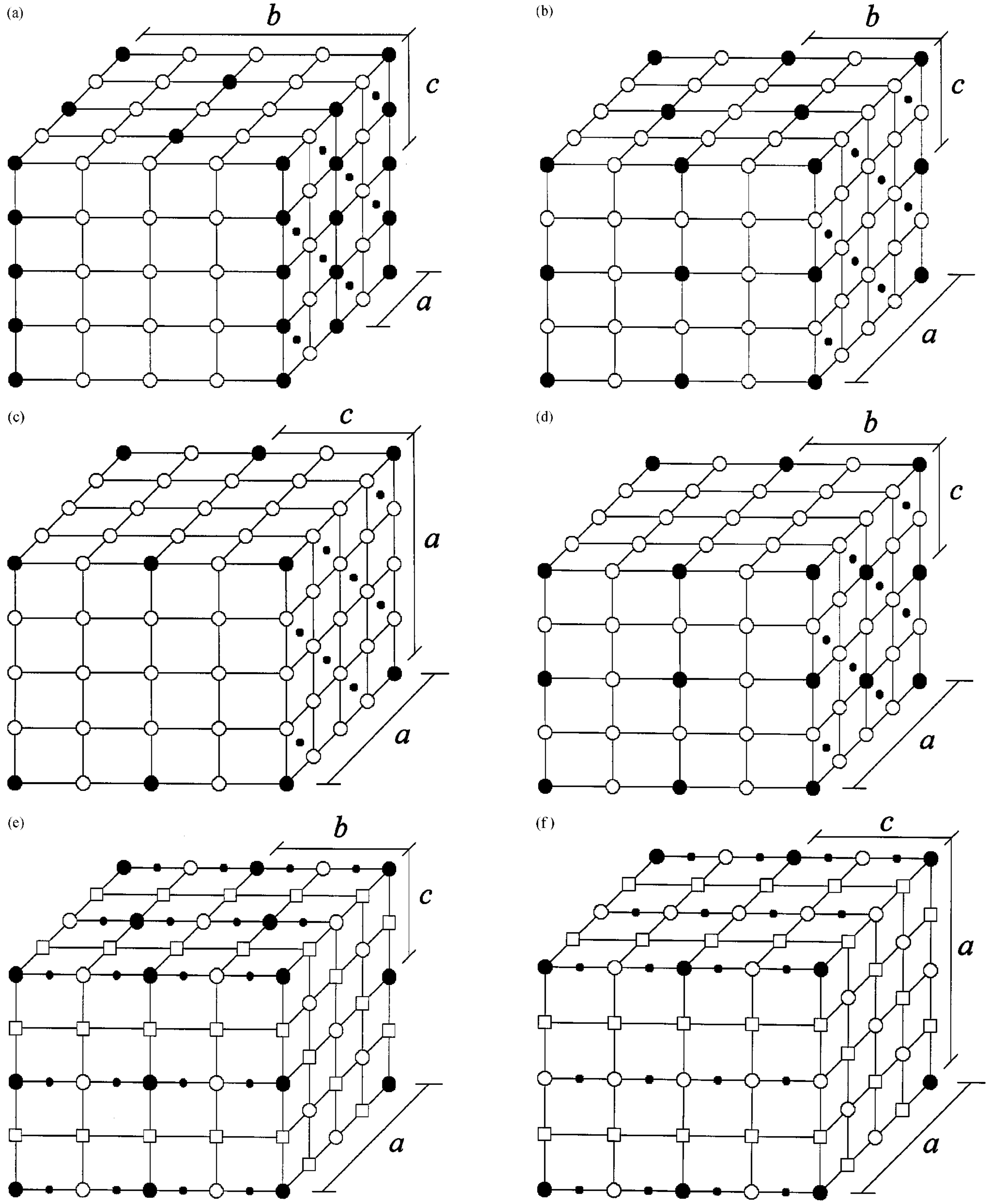

FIG. 1. Proposed oxygen-vacancy ordering schemes for $Sr_nFe_nO_{3n-1}$ ($n = 2, 4$, and 8). (a) $Sr_2Fe_2O_5$ brownmillerite *I*-centered unit cell, (b) $Sr_4Fe_4O_{11}$ *C*-centered unit cell proposed by Takano (13), (c) $Sr_8Fe_8O_{23}$ *I*-centered unit cell proposed by Takano, (d) $Sr_4Fe_4O_{11}$ *B*-centered unit cell proposed by Gibb (28), (e) $Sr_4Fe_4O_{11}$ new *C*-centered unit cell, and (f) $Sr_8Fe_8O_{23}$ new *I*-centered unit cell. The open circles, filled circles, small filled circles, and open squares indicate O^{2-} anions, vacancies, Fe cations, and Sr^{2+} cations, respectively.

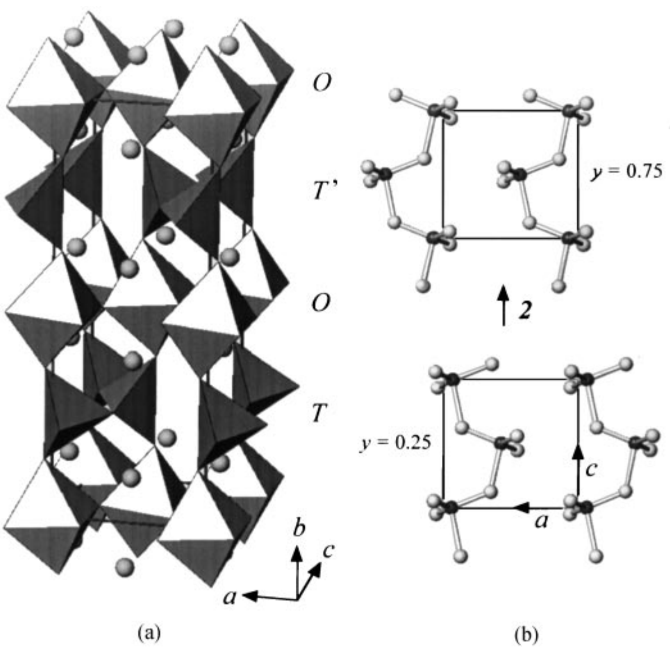

FIG. 2. Schematic representation of an $A_2B_2O_5$ brownmillerite unit cell with *Ibm*2 crystal symmetry (a) and associated expanded views of the $y = 0.25$ (T) and $y = 0.75$ (T') BO_4 tetrahedra layers (b) to emphasize the symmetry relationship between these T and T' layers.

with the space group *Icmm* (23, 24). All five $A_2B_2O_5$ compounds exhibit strong antiferromagnetic coupling and a *G*-type spin structure to high temperatures ($330\ \mathrm{K} \leq T_N \leq 725\ \mathrm{K}$) (21, 23–27).

For the phases $Sr_4Fe_4O_{11}$ ($n = 4$) and $Sr_8Fe_8O_{23}$ ($n = 8$), *C*-centered $2\sqrt{2}a_p \times 2a_p \times \sqrt{2}a_p$ and *I*-centered $2\sqrt{2}a_p \times 2\sqrt{2}a_p \times 2a_p$ unit cells, respectively, were determined from electron and X-ray diffraction measurements (12). Using these unit cells as templates, in which the oxygen-vacancy sites considered alone constitute the requisite Bravais lattice, structural models for $Sr_4Fe_4O_{11}$ and $Sr_8Fe_8O_{23}$ were subsequently proposed by Takano *et al.* (13). Schematic representations of the Takano oxygen-vacancy ordering schemes proposed for $Sr_4Fe_4O_{11}$ and $Sr_8Fe_8O_{23}$ are shown in Figs. 1b and 1c. Tofield *et al.* (9) had previously proposed a structure for $Sr_4Fe_4O_{11}$ with identical vacancy ordering, but a doubled *z*-axis unit-cell size. More recently, Gibb (28) has reinvestigated the $Sr_4Fe_4O_{11}$ phase. From X-ray powder diffraction data a $2\sqrt{2}a_p \times 2a_p \times \sqrt{2}a_p$ unit-cell size was confirmed; however, the presence of a very weak (010) reflection caused us to question the validity of the *C*-centered crystal symmetry previously put forward. To account for the unusual magnetic properties of $Sr_4Fe_4O_{11}$ (10, 13), Gibb proposed a new structural model in which layers of $Fe^{3+}O_6$ octahedra are separated by layers of $Fe^{4+}O_5$ square pyramids. A schematic representation of the proposed oxygen-vacancy ordering scheme is shown in Fig. 1d. This Gibb model is closely related to the Takano model for $Sr_4Fe_4O_{11}$; when the oxygen-vacancy sites are considered alone they form a *B*-centered, rather than *C*-centered, Bravais lattice of identical unit-cell size. Cooperative tilting and/or other distortions can lower the crystal symmetry in both cases to primitive. Therefore, both vacancy ordered models are viable candidates for the crystal structure of $Sr_4Fe_4O_{11}$.

In the oxygen-vacancy ordering schemes proposed by Takano, the vacancies are ordered at every $n/2$ site in lines of $[101]_p$ direction. In Fig. 3a the ordering of vacancies along such a line within an SrO_3 layer is depicted for the proposed $Sr_4Fe_4O_{11}$ model. These lines of ordered oxygen atoms and vacancies are themselves ordered with respect to one another to yield the final supercells. However, in the case of $Sr_4Fe_4O_{11}$ and $Sr_8Fe_8O_{23}$, unlike $Sr_2Fe_2O_5$, the

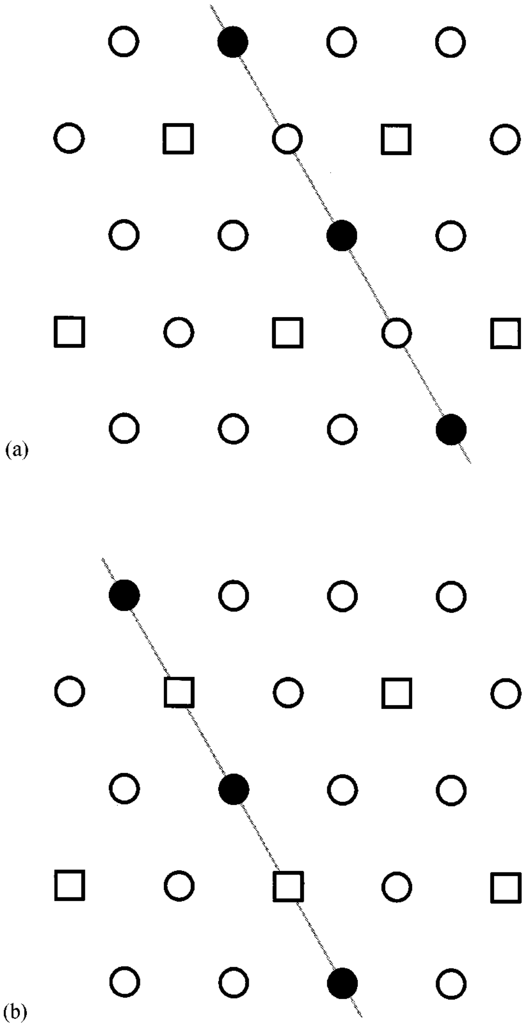

FIG. 3. Schematic representations of the ordering of oxygen vacancies along a line of direction $[101]_p$ within an originally SrO_3 layer. (a) The scheme proposed by Takano for $Sr_4Fe_4O_{11}$, and (b) the alternate placement of the oxygen-vacancy-ordered $[101]_p$ line for $Sr_4Fe_4O_{11}$. The open circles, filled circles, and open squares indicate O^{2-} anions, vacancies, and Sr^{2+} cations, respectively.

placement of the vacancy-ordered $[101]_p$ line within an SrO_3 layer is not unique. As shown in Fig. 3b, an alternate placement for the $[101]_p$ ordered line of vacancies exists. Upon adopting this alternative line for the vacancy ordering in both $Sr_4Fe_4O_{11}$ and $Sr_8Fe_8O_{23}$, one obtains new vacancy ordering schemes. Schematic representations of these new vacancy ordering schemes for $Sr_4Fe_4O_{11}$ and $Sr_8Fe_8O_{23}$ are shown in Figs. 1e–1f. Considered by themselves, the oxygen vacancies in both the Takano and the alternate schemes are ordered identically, forming a C-centered $2\sqrt{2}a_p \times 2a_p \times \sqrt{2}a_p$ or I-centered $2\sqrt{2}a_p \times 2\sqrt{2}a_p \times 2a_p$ unit cell. Since all the oxygen atoms are crystallographically equivalent in the aristotype $SrFeO_3$, it is simply the orientation of the $Sr_4Fe_4O_{11}$ and $Sr_8Fe_8O_{23}$ supercells with respect to the underlying perovskite crystal structure that differs between the Takano and the new schemes.

CRYSTAL STRUCTURE DETERMINATION

$SrFeO_3$ ($n = \infty$)

An excellent fit between the observed powder diffraction data and calculated profile of $SrFeO_3$ was achieved using a simple cubic perovskite model ($S = 1.616$, $S = R_{wp}/R_e$). In the first stage of the refinement, the three Debye–Waller parameters of the Sr, Fe, and O atoms were constrained to be isotropic. Upon convergence, this constraint was removed and the refinement was continued with anisotropic Debye–Waller parameters. Significant deviation from isotropic thermal motion was revealed for the oxygen atoms. During the final stage of the refinement, the Debye–Waller parameters of the Sr and Fe atoms were constrained to be isotropic. The final neutron powder diffraction profiles and refined crystallographic parameters for $SrFeO_3$ are presented in Fig. 4 and Table 1. Throughout the refinement, the

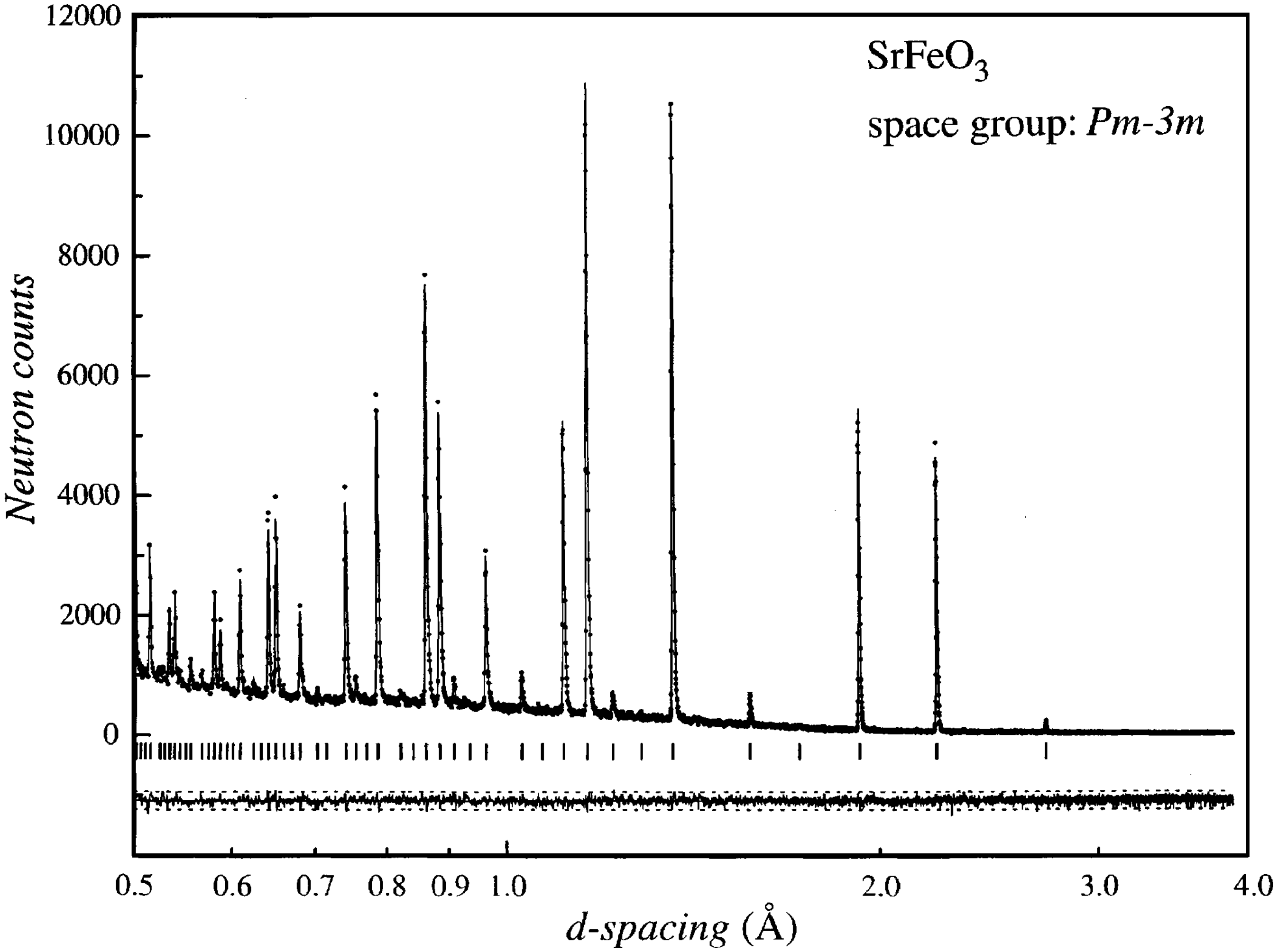

FIG. 4. Neutron powder diffraction data and Rietveld refinement profile for $SrFeO_3$ refined in the $Pm\bar{3}m$ space group. Dots are the raw observed data. The solid line is the calculated profile. Tic marks below the profile mark the positions of all allowed reflections. The difference between the observed and calculated profiles is plotted at the bottom in units of difference divided by estimated standard deviation (which is the square root of the observed counts). The dotted lines above and below the difference/esd line are + 5 and − 5 in these units.

TABLE 1
Structural Parameters for $SrFeO_3$ Refined in Space Group $Pm\bar{3}m$

Atom	Site	x	y	z	U_{iso} or $u_{ij} \times 10^2$ (Å^2)
Sr	1*b*	1/2	1/2	1/2	0.7(1)
Fe	1*a*	0	0	0	0.4(1)
O	3*d*	0	0	1/2	$u_{11} = 1.2(1)$, $u_{33} = 0.6(1)$

Note. $a = 3.851(1)$ Å.
$R_{wp} = 0.099$, $R_p = 0.063$, $R_e = 0.061$, $R_I = 0.065$, $S = 1.616$.

oxygen fractional site occupancy was fixed at unity. No evidence suggestive of a lower crystal symmetry, such as splitting of diffraction peaks, unusual peak broadening, or weak superlattice peaks, was detected.

The observed simple cubic perovskite structure of $SrFeO_3$ confirms the absence of a static cooperative Jahn–Teller distortion (1, 29). Normally a Jahn–Teller effect would be expected of a high-spin transition-metal d^4 cation in octahedral coordination. The possibility exists, however, that a dynamic or an incoherent static Jahn–Teller effect is present, since these are not ruled out by an average primitive cubic symmetry. If dynamic or incoherent Jahn–Teller distortions are present in $SrFeO_3$, then it is expected that the oxygen atoms will appear to exhibit anomalously large thermal motion along Fe–O directions. The structural refinement of $SrFeO_3$, however, shows that the largest thermal motion of the oxygen anions is perpendicular to the Fe–O directions ($u_{11} = 0.012(1)$ Å^2) and not parallel ($u_{33} = 0.006(1)$ Å^2). This is as expected for thermal librational motion of the FeO_6 octahedra. Thus, the anisotropic Debye–Waller parameters observed in $SrFeO_3$ present no evidence for a dynamic or incoherent Jahn–Teller effect.

$Sr_8Fe_8O_{23}$ ($n = 8$)

Initial analysis of the $Sr_8Fe_8O_{23}$ neutron powder diffraction data indicated that the proposed tetragonal *I*-centered $2\sqrt{2}a_p \times 2\sqrt{2}a_p \times 2a_p$ unit cell was consistent with all the observed diffraction peaks. The ideal, i.e., before relaxation, $Sr_8Fe_8O_{23}$ structural model proposed by Takano and the new vacancy-ordered model (see Fig. 1c and 1f) are described by the monoclinic $I112/m$ and tetragonal $I4/mmm$ space groups, respectively. Furthermore, the ideal $Sr_8Fe_8O_{23}$ structure proposed by Takano can be equivalently described in the orthorhombic *Fmmm* space group with an enlarged $4a_p \times 4a_p \times 2a_p$ unit cell. Of relevance to the crystal structure determination of $Sr_8Fe_8O_{23}$, the $I112/m$ and *Fmmm* space group crystallographic models differ in the atomic relaxation displacements allowed. Henceforth, each structural model of $Sr_8Fe_8O_{23}$ (and $Sr_4Fe_4O_{11}$) will be referred to by its corresponding space group symbol.

TABLE 2
Structural Parameters for $Sr_8Fe_8O_{23}$ Refined in Space Group $I4/mmm$

Atom	Site	x	y	z	$U_{iso} \times 10^2$ (Å^2)
Sr(1)	8*i*	0.2577(3)	0	0	0.6(1)
Sr(2)	8*j*	0.2510(3)	0	1/2	0.8(1)
Fe(1)	4*e*	0	0	0.250(2)	0.8(3)
Fe(2)	8*f*	1/4	1/4	1/4	0.3(2)
Fe(3)	4*d*	1/2	0	1/4	0.1(2)
O(1)	2*b*	0	0	1/2	1.0(2)
O(2)	16*m*	0.1190(2)	0.1190(2)	0.2224(3)	0.9(1)
O(3)	8*h*	0.2340(3)	0.2340(3)	1/2	0.6(1)
O(4)	16*k*	0.1237(2)	0.6237(2)	1/4	0.8(1)
O(5)	4*c*	1/2	0	0	1.1(1)

Note. $a = 10.929(1)$ Å, $c = 7.698(1)$ Å.
$R_{wp} = 0.085$, $R_p = 0.053$, $R_e = 0.054$, $R_I = 0.060$, $S = 1.577$.

Crystal structure refinements were performed using the $I4/mmm$, *Fmmm*, and $I112/m$ models for $Sr_8Fe_8O_{23}$. The initial atomic coordinates used corresponded to the respective ideal structures and the Debye–Waller parameters of all atoms were constrained to be isotropic. In Tables 2–4 the final obtained crystallographic parameters for the $I4/mmm$, $I112/m$, and *Fmmm* model refinements of $Sr_8Fe_8O_{23}$ are listed.

An excellent fit between the observed neutron diffraction data and calculated profile for $Sr_8Fe_8O_{23}$ was obtained with the $I4/mmm$ structural model ($S = 1.577$) (see Fig. 5), suggesting that this is the correct structure, whereas for the $I112/m$ and *Fmmm* structural models ($S = 1.694$ and 1.686) statistically significant errors between the observed and

TABLE 3
Structural Parameters for $Sr_8Fe_8O_{23}$ Refined in Space Group $I112/m$

Atom	Site	x	y	z	$U_{iso} \times 10^2$ (Å^2)
Sr(1)	8*j*	0.379(1)	0.124(2)	0.254(2)	0.2(1)
Sr(2)	8*j*	0.879(1)	0.122(2)	0.230(1)	0.6(1)
Fe(1)	4*i*	0.134(4)	0.124(5)	0	0.1(4)
Fe(2)	4*i*	0.634(3)	0.130(4)	0	0.3(7)
Fe(3)	4*i*	0.376(5)	0.382(5)	0	0.3(5)
Fe(4)	4*i*	0.118(3)	0.619(4)	0	0.0(7)
O(1)	8*j*	0.117(2)	0.117(2)	0.223(1)	1.9(2)
O(2)	8*j*	0.626(2)	0.124(2)	0.253(4)	1.1(1)
O(3)	4*i*	0.265(1)	0.008(2)	0	0.1(2)
O(4)	4*i*	0	1/4	0	1.9(4)
O(5)	2*d*	1/2	0	0	0.9(6)
O(6)	2*c*	0	1/2	0	2.3(9)
O(7)	4*i*	0.258(2)	0.255(2)	0	0.5(3)
O(8)	4*i*	1/2	1/4	0	1.0(5)
O(9)	4*i*	1/4	1/2	0	0.6(5)
O(10)	2*b*	1/2	1/2	0	1.3(4)
O(11)	4*i*	0.737(2)	0.261(2)	0	1.1(4)

Note. $a = 10.928(3)$ Å, $b = 10.928(3)$ Å, $c = 7.698(1)$Å, $\gamma = 90.01(1)°$.
$R_{wp} = 0.091$, $R_p = 0.056$, $R_e = 0.054$, $R_I = 0.056$, $S = 1.694$.

TABLE 4
Structural Parameters for $Sr_8Fe_8O_{23}$ Refined in Space Group *Fmmm*

Atom	Site	x	y	z	$U_{\mathrm{iso}} \times 10^2$ (Å^2)
Sr(1)	16*k*	1/4	0.1283(6)	0.25	0.2(1)
Sr(2)	16*m*	0	0.1216(7)	0.2282(7)	0.6(1)
Fe(1)	8*g*	0.132(1)	0	0	0.2(3)
Fe(2)	8*g*	0.377(2)	0	0	0.7(4)
Fe(3)	16*o*	0.128(1)	0.248(1)	0	0.1(2)
O(1)	16*o*	0.1321(6)	0.1272(8)	0	1.2(1)
O(2)	8*e*	1/4	1/4	0	1.2(2)
O(3)	16*o*	0.3742(6)	0.124(1)	0	0.8(1)
O(4)	8*g*	0.257(1)	0	0	0.7(3)
O(5)	4*b*	1/2	0	0	1.3(3)
O(6)	16*l*	0.1250(7)	1/4	1/4	1.2(1)
O(7)	16*n*	0.117(1)	0	0.224(1)	1.9(2)
O(8)	8*h*	0	0.263	0	0.5(3)

Note. $a = 15.453(3)$ Å, $b = 15.457(3)$ Å, $c = 7.698(1)$ Å.
$R_{\mathrm{wp}} = 0.090$, $R_{\mathrm{p}} = 0.056$, $R_{\mathrm{e}} = 0.054$, $R_{\mathrm{I}} = 0.058$, $S = 1.686$.

calculated intensities of several reflections were evident (see Figs. 6 and 7). In these plots the difference divided by estimated standard deviation is displayed (as opposed to the commonly plotted difference) to emphasize the error between the observed and calculated diffraction patterns. It is interesting to see, in Figs. 5–7, how subtle the difference in *goodness of fit* is between these three crystal structure models of $Sr_8Fe_8O_{23}$. In addition to the small errors in diffraction pattern fits, the *I*112/*m* and *Fmmm* refined crystal structures both include oxygen atoms with anomalously large Debye–Waller parameters ($U_{\mathrm{iso}} > 0.015$ Å^2) (see Tables 3 and 4), further suggesting that the *I*112/*m* and *Fmmm* crystallographic models are incorrect.

With regard to the general problem of determining crystal structures *ab initio* from powder diffraction data, the *I*112/*m* and *Fmmm* refinements illustrate how incorrect crystal structures can, sometimes, fit the observed powder diffraction data satisfactorily and yield acceptably low agreement factors (R_{wp}, R_{I}, etc). Pointedly, one should seek more than just good agreement factors before concluding that a specific structural model is correct. Satisfying this requirement, conclusive evidence confirming the correctness of the *I*4/*mmm* crystal structure is presented in a section below on Fe–O and O–O bond-length distributions in $Sr_4Fe_4O_{11}$ and $Sr_8Fe_8O_{23}$.

$Sr_4Fe_4O_{11}$ (n = 4)

The neutron powder diffraction pattern of $Sr_4Fe_4O_{11}$ was indexed using the proposed orthorhombic *C*-centered $2\sqrt{2}a_{\mathrm{p}} \times 2a_{\mathrm{p}} \times \sqrt{2}a_{\mathrm{p}}$ unit cell. The observation of the $h + k = 2n$ extinction condition rules out a *B*-centered $2\sqrt{2}a_{\mathrm{p}} \times 2a_{\mathrm{p}} \times \sqrt{2}a_{\mathrm{p}}$ unit cell for $Sr_4Fe_4O_{11}$; however, this does not disprove the oxygen-vacancy ordering scheme put forward by Gibb (28). The ideal $Sr_4Fe_4O_{11}$ structural model proposed by Takano and the new vacancy-ordered model (see Figs. 1b and 1e) are described by the monoclinic *C*12/*m*1 and orthorhombic *Cmmm* space groups, respectively. For the *C*12/*m*1 and *Cmmm* crystal structure refinements of $Sr_4Fe_4O_{11}$, the initial atomic coordinates used corresponded to the respective ideal structures and the Debye–Waller parameters of all atoms were constrained to be isotropic.

An excellent fit between the observed diffraction data and calculated profile was obtained with the *Cmmm* structural model ($S = 1.620$) (see Fig. 8), whereas for the *C*12/*m*1 model ($S = 1.920$), intensity errors for several reflections (see Fig. 9) were clearly apparent. The final obtained crystallographic parameters for the *Cmmm* and *C*12/*m*1 model refinements are listed in Tables 5 and 6. It therefore appears from a comparison of the obtained neutron diffraction profile fits and agreement factors that the orthorhombic *Cmmm* crystallographic model of $Sr_4Fe_4O_{11}$ is correct, while the initially proposed monoclinic *C*12/*m*1 model is incorrect. Further support for this conclusion, which is presented in the following section, is provided by the Fe–O and O–O bond-length distributions obtained from the refined *C*12/*m*1 and *Cmmm* crystal structures.

The refined *Cmmm* crystal structure of $Sr_4Fe_4O_{11}$, which is shown in Fig. 10a, consists of one-dimensional chains of vertex-linked FeO_6 octahedra cross-linked by $(FeO_5)_2$ "bow-tie" dimer units. For comparison with $Sr_4Fe_4O_{11}$, the refined *I*4/*mmm* crystal structure of $Sr_8Fe_8O_{23}$ is shown in Fig. 10b. Interestingly, if, starting with $Sr_4Fe_4O_{11}$, one converts alternate $[001]_{\mathrm{p}}$ lines of $(FeO_5)_2$ bow-tie units into chains of FeO_6 octahedra by selectively filling oxygen vacancies, one obtains very closely the crystal structure of $Sr_8Fe_8O_{23}$. This close structural relationship between $Sr_4Fe_4O_{11}$ and $Sr_8Fe_8O_{23}$ is consistent with the ease of interconverting the phases by low-temperature annealing.

Fe–O AND O–O BOND-LENGTH DISTRIBUTIONS IN $Sr_4Fe_4O_{11}$ AND $Sr_8Fe_8O_{23}$

An analysis of the distribution of Fe–O bond lengths and O–O distances was used to confirm the validity of the structural models for $Sr_4Fe_4O_{11}$ and $Sr_8Fe_8O_{23}$.

The distributions of Fe–O and O–O bond lengths obtained for the $Sr_4Fe_4O_{11}$ and $Sr_8Fe_8O_{23}$ crystal structure refinements are displayed in Fig. 11. The very broad Fe–O and O–O bond length distributions observed for the *C*12/*m*1, *I*112/*m*, and *Fmmm* models (Figs. 11a–11c) are unusual and suggest that these crystal structure models are incorrect. A second alarming feature of these three model refinements is the significant fraction of short (~2.60 Å) O–O interatomic distances observed. However, it is the

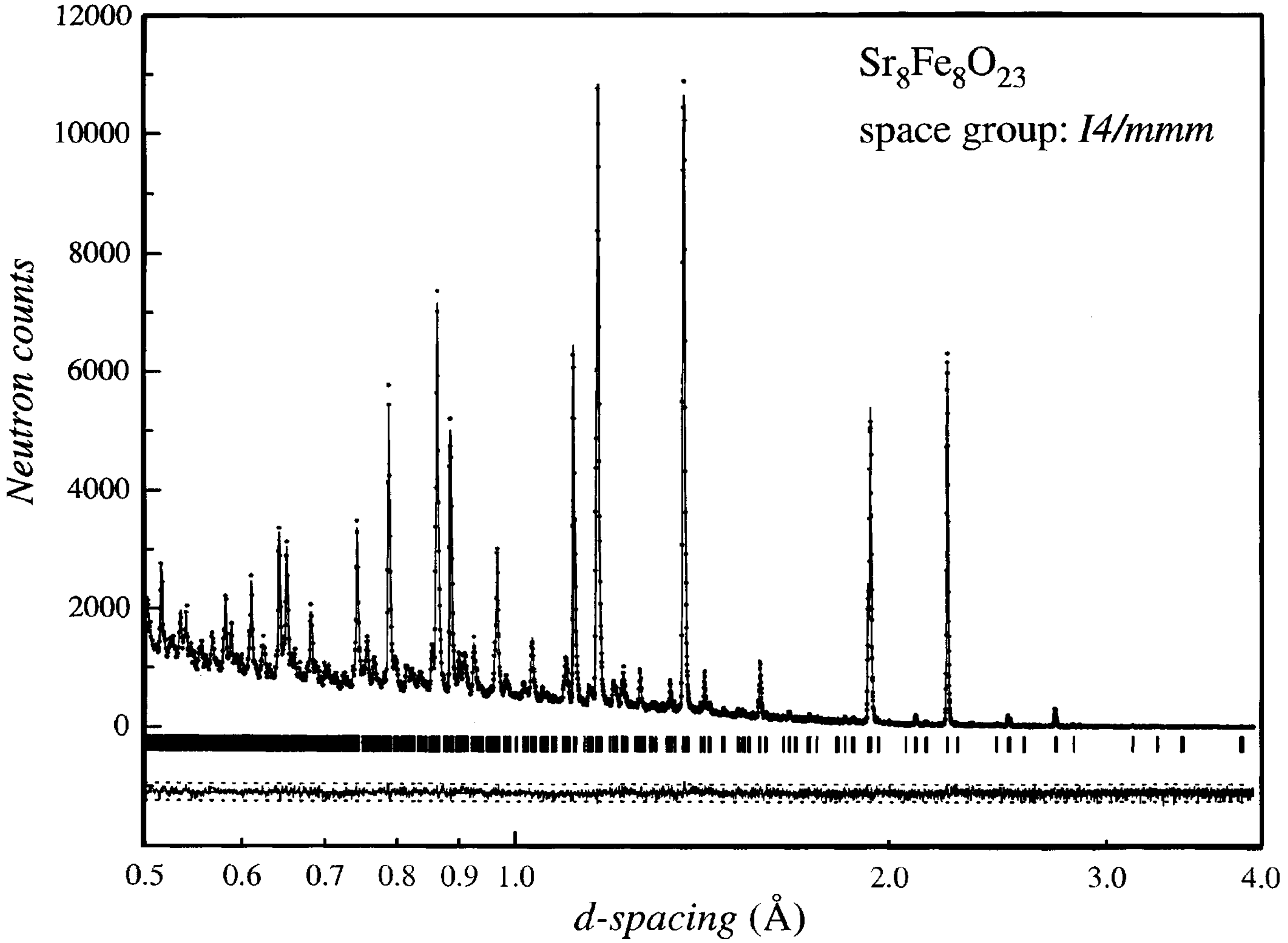

FIG. 5. Neutron powder diffraction data and Rietveld refinement profile for $Sr_8Fe_8O_{23}$ refined in the *I*4/*mmm* space group. Format is the same as for Fig. 4.

common presence of an unaccountably short Fe–O bond, d(Fe–O) < 1.75 Å, that effectively disproves the proposed *C*12/*m*1, *I*112/*m*, and *Fmmm* models. The shortest Fe–O bond lengths typically observed in mixed alkaline-earth iron oxide compounds are ~1.85(2) Å.

The validity of the refined *Cmmm* $Sr_4Fe_4O_{11}$ and *I*4/*mmm* $Sr_8Fe_8O_{23}$ crystal structures is affirmed by their Fe–O and O–O bond-length distributions (Figs. 11d and 11e). Three common features define the bond-length distributions of $Sr_4Fe_4O_{11}$ and $Sr_8Fe_8O_{23}$. All the Fe–O bond lengths and a high proportion of the O–O interatomic distances are distributed in the normal ranges of 1.85–2.05 Å and 2.70–2.90 Å. Contrasting the competing *C*12/*m*1, *I*112/*m*, and *Fmmm* refined structural models, there are no exceptionally short Fe–O bonds. There are present, however, a number of short O–O interatomic distances of length ~2.60 Å. In both crystal structures, these short O–O distances define the square-bases of the FeO_5 polyhedra. Presumably, for the square-pyramid FeO_5 units the increased repulsion energy due to short O_b–O_b distances is compensated by a greater relief in O_a–O_b repulsion energy (O_a and O_b refer to apical and basal oxygen atoms, respectively).

$Sr_2Fe_2O_5$ (n = 2)

In consideration of possible structural disorder in $Sr_2Fe_2O_5$ (21), the crystal and magnetic structures of $Sr_2Fe_2O_5$ were refined in both the space groups *Ibm*2 and *Icmm*. For each refinement the Fe^{3+} magnetic moments were constrained to lie parallel to the z-axis, and the Debye–Waller parameters were constrained to be isotropic.

The best agreement between the observed diffraction data and calculated profile was achieved with the disordered *Icmm* structural model of $Sr_2Fe_2O_5$ ($S = 1.652$ for *Icmm* vs

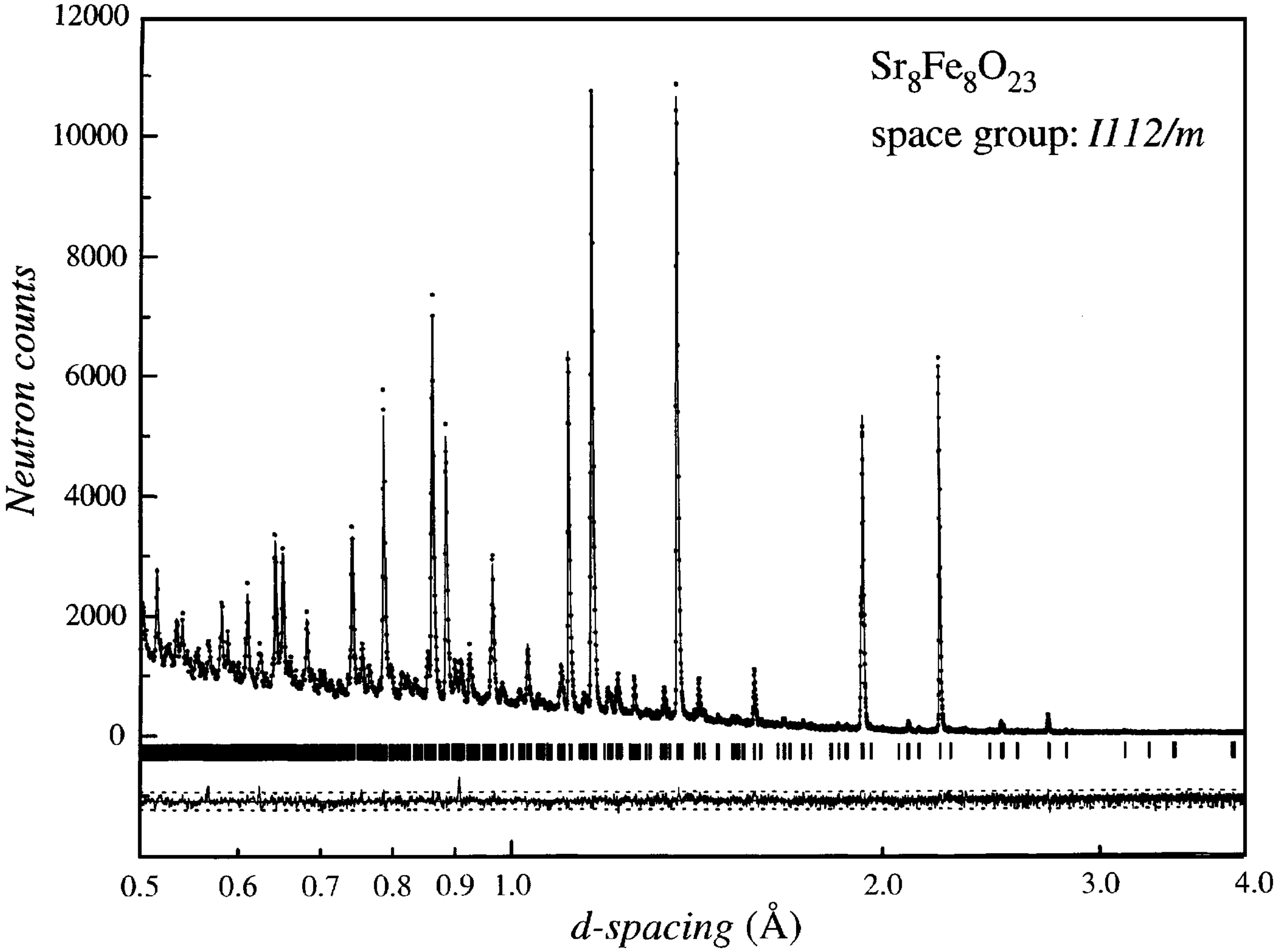

FIG. 6. Neutron powder diffraction data and Rietveld refinement profile for $Sr_8Fe_8O_{23}$ refined in the *I*112/*m* space group. This model was shown to be incorrect. Format is the same as for Fig. 4.

1.717 for *Ibm*2). The final neutron powder diffraction profiles and crystallographic parameters for $Sr_2Fe_2O_5$ refined in space group *Icmm* are presented in Fig. 12 and Table 7. As previously suggested (21), this disorder is probably limited to the irregular occurrence of a $\bar{1}$ symmetry relation between adjacent *T* and *T′* FeO_4 layers. In regions free of such stacking errors the crystal symmetry is anticipated to be *Ibm*2. Different synthesis conditions, superior crystallinity, fewer stacking errors, and, therefore, overall greater structural order may explain the assignment of the *Ibm*2 space group to a single crystal of $Sr_2Fe_2O_5$ (22).

The difference in fits between the disordered and ordered structural models of $Sr_2Fe_2O_5$ was small. However, additional support for concluding a disordered *Icmm* model is provided by the refined magnetic moments (23). The octahedral Fe(1) and tetrahedral Fe(2) site magnetic moments refined to values of 4.0(2) μ_B and 3.7(1) μ_B, respectively, for both the ordered and disordered structural models. These values are low when compared with the Fe^{3+} magnetic moment of 4.5(2) μ_B found in the fully ordered $Ca_2Fe_2O_5$ compound (26, 27). Considering that neutron diffraction measures only the magnetic component exhibiting long-range order, and Mössbauer spectroscopy has determined very similar internal magnetic flux densities for both $Ca_2Fe_2O_5$ and $Sr_2Fe_2O_5$ ($B_{oct} = 51(1)$ T and $B_{tetra} = 43(1)$ T) (30), the low moments observed for $Sr_2Fe_2O_5$ can therefore be attributed to the presence of structural disorder and the resulting imperfect alignment of magnetic spins. The structural disorder perturbs the magnetic interactions locally, resulting in incoherent and coherent components along the *x*- and *z*-axes, respectively. This picture of structural disorder leading to imperfect spin alignment is consistent with the Fe(2) tetrahedral site cations having the most reduced "ordered" magnetic moment, 3.7 μ_B vs 4.0 μ_B, since the FeO_4 layer is effectively the origin of the disorder.

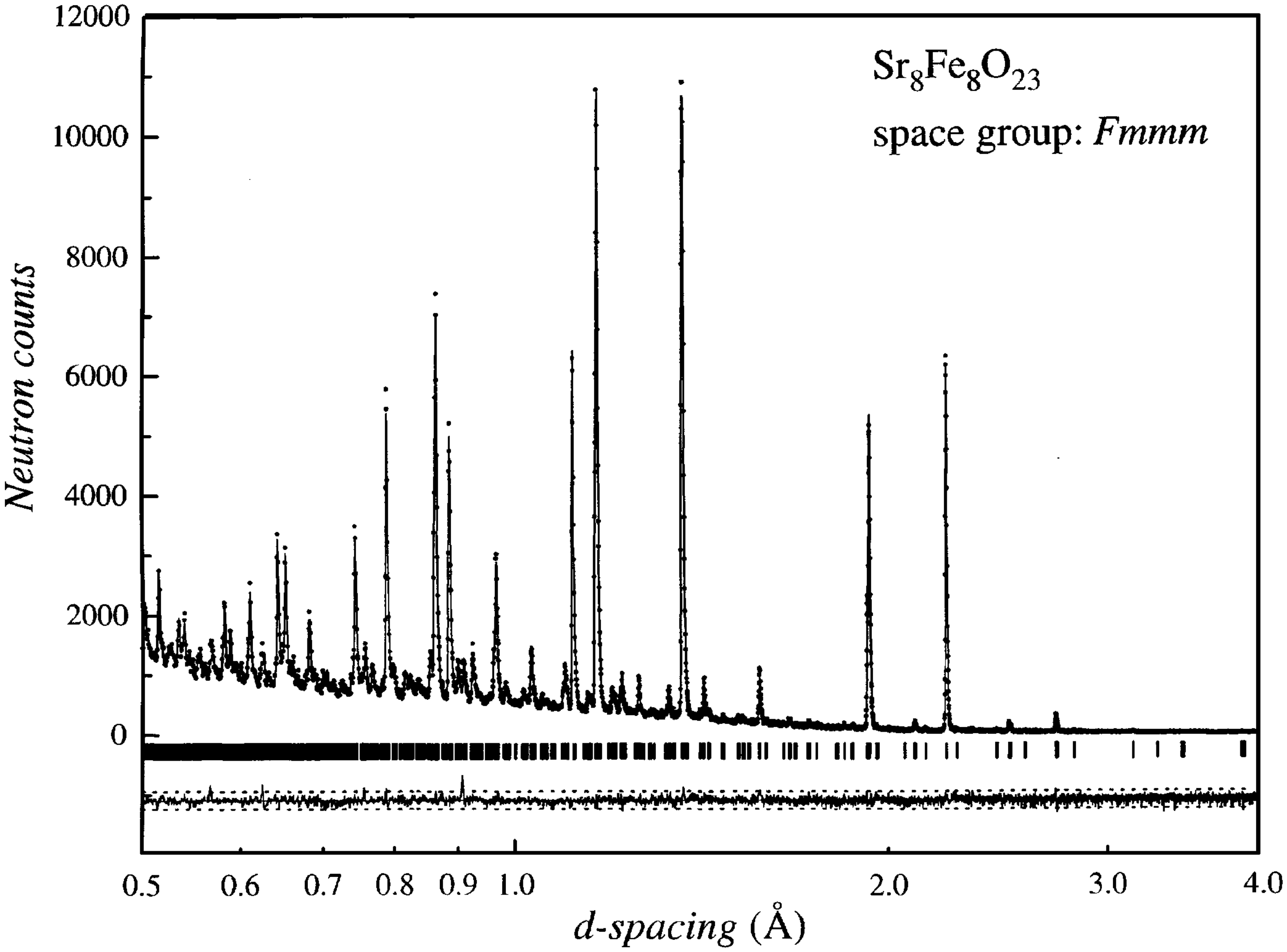

FIG. 7. Neutron powder diffraction data and Rietveld refinement profile for $Sr_8Fe_8O_{23}$ refined in the *Fmmm* space group. This model was shown to be incorrect. Format is the same as for Fig. 4.

Relationship between Crystal Structure and the Electronic and Magnetic Properties of $Sr_4Fe_4O_{11}$ and $Sr_8Fe_8O_{23}$

Before commencing the discussion of the relationship between structure and electronic properties of $Sr_4Fe_4O_{11}$ and $Sr_8Fe_8O_{23}$, it is beneficial to first consider the general systematics for the electronic properties of first-row transition-metal compounds as have been elaborated by Zaanen *et al.* and Fujimori (31, 32). The electronic behavior of transition-metal compounds is governed by the relative magnitudes of the on-site electron–electron correlation energy U, the charge-transfer energy Δ, the $B{:}3d$–O$:2p$ hybridization strength T_{pd} which reflects the covalency of the B–O bonding (B is the transition metal), and the bandwidths W_p and W_d. The U and Δ energies are associated with charge fluctuations of the type $d^n + d^n : d^{n+1} + d^{n-1}$ which involve the d-d Coulomb and exchange interactions, and $d^n \leftrightarrow d^{n+1}L^{-1}$, where L^{-1} denotes a hole in the anion valence band. The magnitude of Δ is directly related to the electronegativity of the anion and the Mandelung potential, both of which tend to stabilize an ionic ground state and a noble-gas valence configuration of the anion. Whereas the parameters U, Δ, and T_{pd} are essentially determined by local coordination geometry of a single BO_k unit (intracluster coupling), the dispersional widths W_p and W_d associated with the O$:2p$ and $B{:}3d$ bands arise from the coupling of the BO_k units in the crystal structure (intercluster coupling).

In general the anion-to-metal charge-transfer energy Δ decreases from Sc to Cu within the transition metal $3d$ series and with increasing formal oxidation state for a given transition metal (33, 34). These trends combined with the large exchange stabilization of the half-filled $3d^5$ configuration lead to a negative effective Δ value in the case of formally Fe^{4+}-containing $SrFeO_3$, as derived from a cluster model analysis of photoelectron spectra (6). As a result, the

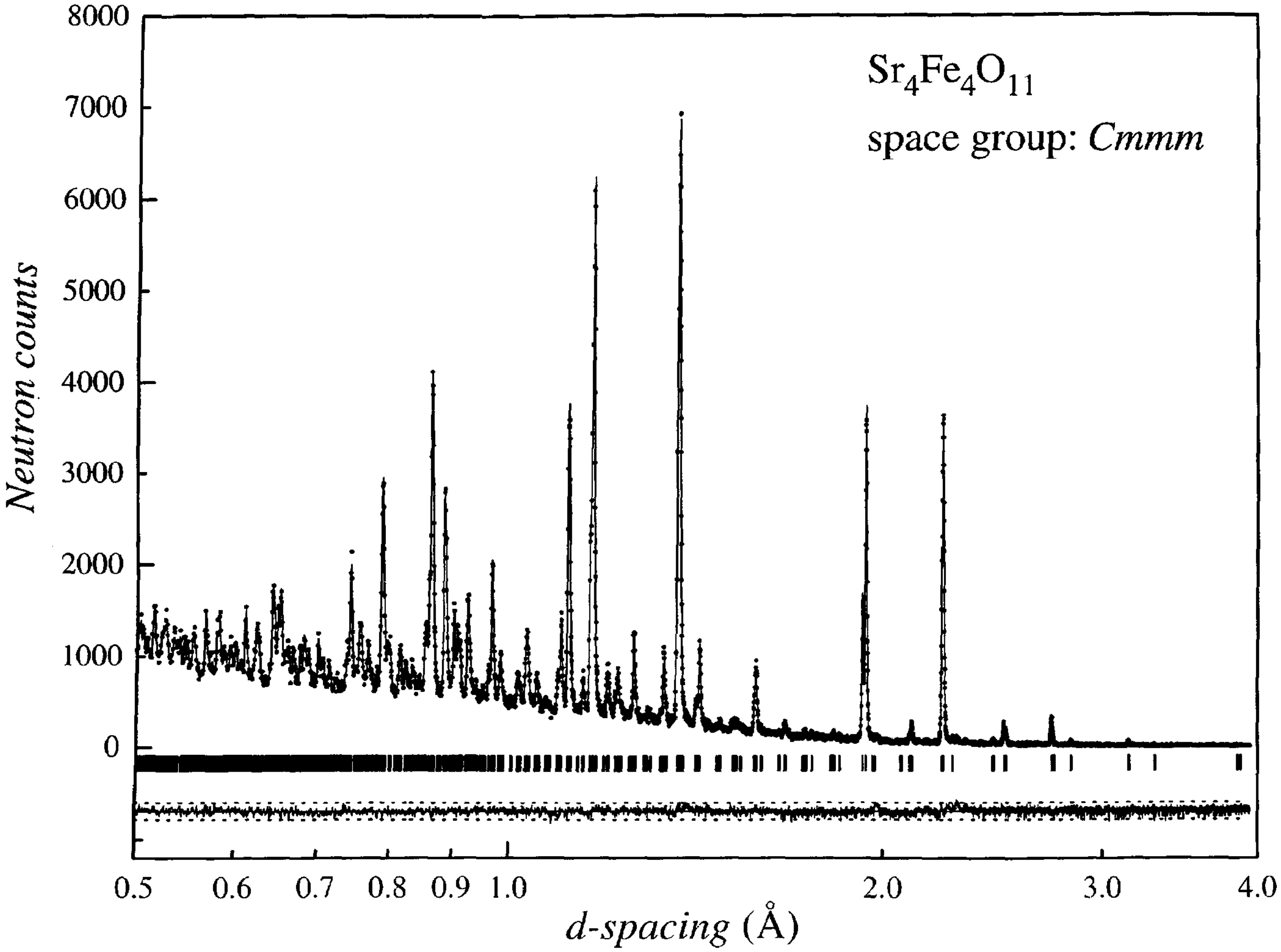

FIG. 8. Neutron powder diffraction data and Rietveld refinement profile for $Sr_4Fe_4O_{11}$ refined in the *Cmmm* space group. Format is the same as for Fig. 4.

electronic ground state of the Fe^{4+} should not be considered as arising from an ionic $3d^4$ configuration, but rather as a mixed covalent state according to

$$\Psi_g = a|d^4\rangle + b|d^5L^{-1}\rangle$$

with a large weight of d^5L^{-1} ($|d^4\rangle$ and $|d^5L^{-1}\rangle$ represent the ionic and covalent limits, respectively).

As suggested by Adler *et al.* (35) the electronic situation in the Fe^{4+}-containing $A_{m+1}Fe_mO_{3m+1}$ ($m = 1$, 2, and ∞) Ruddlesdon–Popper series is characterized by a competition between a local state formally arising from an Fe : d^4 high-spin state and an itinerant continuum state reasonably formulated as d^5L^{-1} with holes having predominantly O : $2p$ character. In the semiconductor Sr_2FeO_4, the local d^4 is the ground state, and is separated by E_{gap} from the d^5L^{-1} continuum, whereas in the three-dimensional perovskite $SrFeO_3$, an increased O : $2p$ bandwidth, W_p, results from the larger number of Fe–O–Fe interactions, compared with the two-dimensional Sr_2FeO_4, and this leads to band-gap closure and a metallic ground state. An important effect of the conduction band in $SrFeO_3$ is to mediate ferromagnetic interactions, which compete with the prevalent Fe–O–Fe antiferromagnetic superexchange interactions, and, consequently, a screw-type spin structure is stabilized below $T_N \approx 130$ K (4).

$Sr_4Fe_4O_{11}$

For the purposes of assigning Fe cation valence states, comparison, and discussion, we present a brief summary of typical Mössbauer measurements (1, 10, 12, 28, 30, 36, 37) of Fe cation isomer shifts (δ) and their relative intensities (measured at ~300 K) for the $Sr_nFe_nO_{3n-1}$ series in Table 8. In constructing this summary, minor components observed only in some studies are presumed to be associated

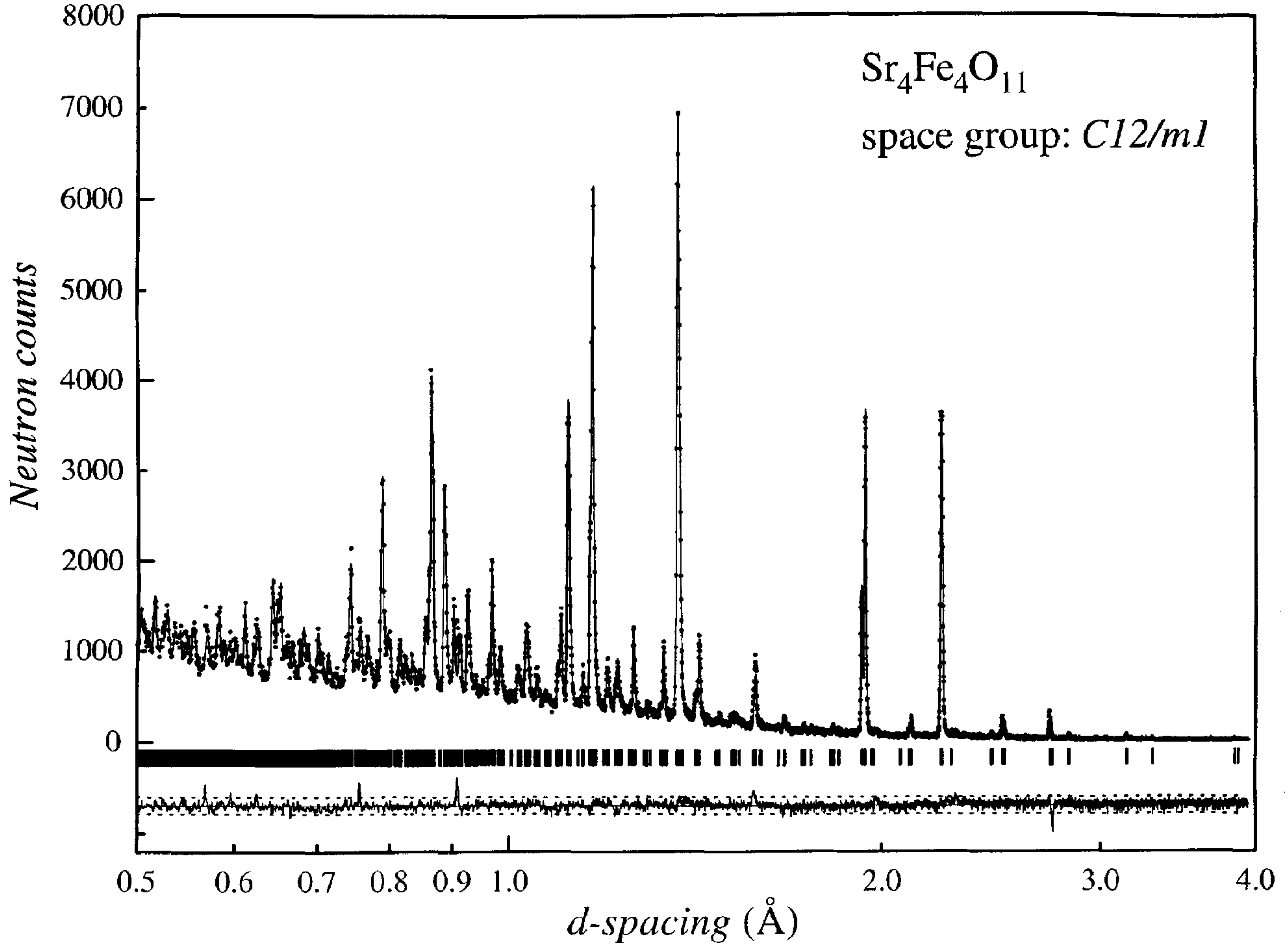

FIG. 9. Neutron powder diffraction data and Rietveld refinement profile for $Sr_4Fe_4O_{11}$ refined in the $C12/m1$ space group. This model was shown to be incorrect. Format is the same as for Fig. 4.

with imperfect oxygen-vacancy ordering and/or secondary phases, have therefore been omitted.

The room-temperature Mössbauer spectrum of $Sr_4Fe_4O_{11}$ consists of two symmetrical doublets of equal intensity. On the basis of the fitted isomer shifts of $\delta = 0.35$ and -0.08 mm s^{-1}, the two components can be assigned to Fe^{3+} and Fe^{4+} cations, respectively. $Sr_4Fe_4O_{11}$, therefore, is a mixed-valence compound. Below a magnetic transition temperature of $T_N \approx 230$ K, the Fe^{3+} component exhibits hyperfine magnetic splitting which saturates at a flux density of $B_{hf} = 46$ T. This value of flux density is indicative of a high-spin d^5 configuration, as a opposed to a low-spin d^5 configuration where a flux density of $B_{hf} \approx 11$ T is expected (approximating $B_{hf} \approx 22\langle S_z \rangle$ T). The magnetic transition appears, from susceptibility data (10), to be antiferromagnetic with some canting of spins in the vicinity of the Néel temperature. For the Mössbauer Fe^{4+} component, a gradual linewidth broadening is observed on cooling to 4 K, but the expected hyperfine splitting associated with magnetic ordering is not observed.

To understand the relationship between crystal structure and the electronic and magnetic properties of $Sr_4Fe_4O_{11}$, a correct assignment of the Fe^{3+} and Fe^{4+} valence states to their respective Fe crystallographic sites is critical. The crystal structure of $Sr_4Fe_4O_{11}$ possesses two distinct Fe sites, Fe(1) and Fe(2), with square-pyramidal and octahedral oxygen coordinations, respectively. It is anticipated, from crystal-field stabilization energy considerations, that the $Fe^{4+}:d^4$ and $Fe^{3+}:d^5$ electronic configurations are best accommodated by the square-pyramidal $Fe(1)O_5$ and octahedral $Fe(2)O_6$ sites, respectively. In opposition to this conclusion, however, we note that the $Fe(2)O_6$ octahedron is compressed with two short and four long Fe–O bonds (see Table 9). This distortion is suggestive of a localized Jahn–Teller effect and therefore a high-spin $Fe^{4+}:d^4$ cation in an octahedral environment. Additionally, compositional

TABLE 5
Structural Parameters for $Sr_4Fe_4O_{11}$ Refined in Space Group *Cmmm*

Atom	Site	x	y	z	$U_{iso} \times 10^2$ (Å^2)
Sr(1)	2*c*	1/2	0	1/2	1.0(1)
Sr(2)	2*d*	0	0	1/2	0.5(1)
Sr(3)	4*g*	0.2588(3)	0	0	0.6(1)
Fe(1)	4*i*	1/2	0.247(1)	0	0.4(1)
Fe(2)	4*f*	1/4	1/4	1/2	0.7(2)
O(1)	2*b*	1/2	0	0	0.6(1)
O(2)	4*h*	0.2695(3)	0	0.5	0.8(1)
O(3)	16*r*	0.3804(2)	0.2761(1)	0.2359(5)	0.9(1)

Note. $a = 10.974(1)$ Å, $b = 7.702(1)$ Å, $c = 5.473(1)$ Å. $R_{wp} = 0.093$, $R_p = 0.056$, $R_e = 0.057$, $R_I = 0.041$, $S = 1.620$.

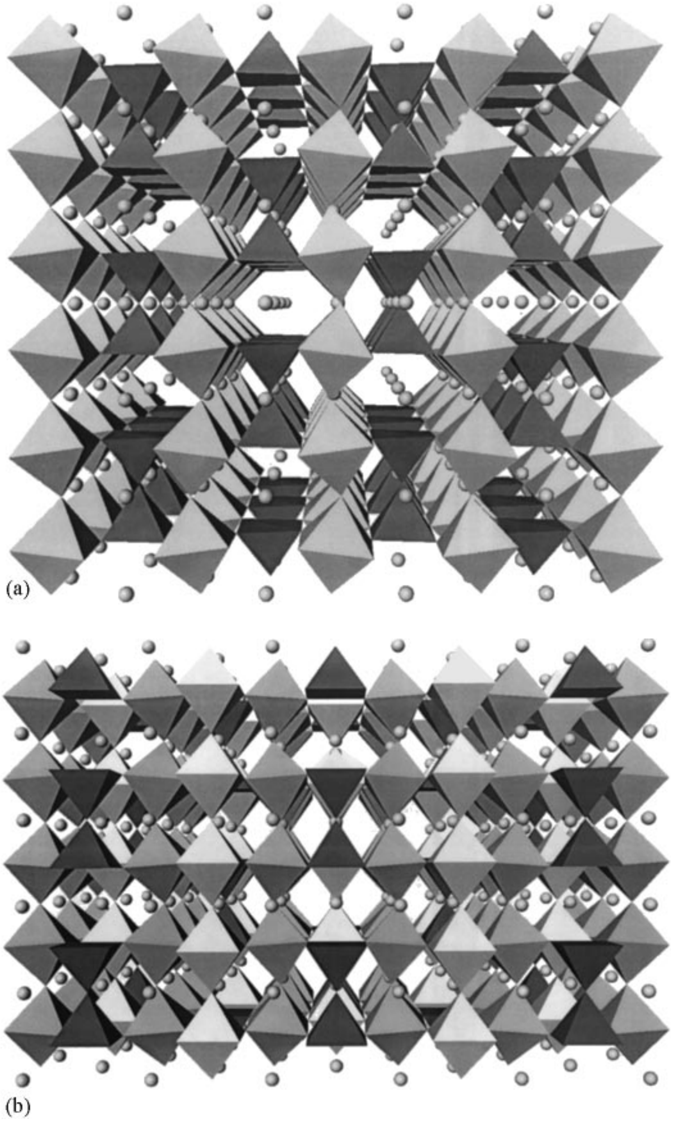

FIG. 10. Crystal structures of $Sr_4Fe_4O_{11}$ (a) and $Sr_8Fe_8O_{23}$ (b) refined in the *Cmmm* and *I*4/*mmm* space groups, respectively.

studies of the related La$MO_{3-\delta}$ (M = Mn, Fe, and Co) perovskites as a function of $p(O_2)$ indicate that M^{2+}–V_O–M^{2+} defect clusters are formed rather than a random distribution of oxygen vacancies and M^{2+} cations (38). If analogous clusters are characteristic of the $SrFeO_x$ system, then in $Sr_4Fe_4O_{11}$ the Fe^{3+} and Fe^{4+} cations are expected to be ordered on the Fe(1) and Fe(2) sites, respectively. As illustrated by these opposing scenarios, the correct assignment of the observed Fe^{3+} and Fe^{4+} valence states to their respective crystallographic Fe sites is nontrivial.

To assign the valence states of the Fe(1) and Fe(2) crystallographic sites, Fe^{3+}–O^{2-} and Fe^{4+}–O^{2-} bond-strength sums were calculated around each Fe cation; these sums are presented in Table 10. The bond-strength calculations were made using the method of Ziólkowski (39). In this approach a bond-length–bond-strength relationship for cation–oxygen bonds is rationalized in terms of an "electrostatic hover model" of the crystal structure. Ions of constant spherical size, ρ_0, are maintained at distances $L = R - \rho_0 - \rho'_0$, where R is the bond length, ρ_0 is the absolute cation radius, and $\rho'_0 = 0.829$ Å is the absolute O^{2-} radius. The bond strength is then given by $s = dz/L$, where z is the formal cation valence and $d = 0.135 - 0.0056z - 0.0347\rho_0 - 0.005z\rho_0$. The relative values of the bond-strength sums, presented in Table 10, clearly indicate that the Fe(1) cation possesses a higher valence state than the Fe(2) cation. Therefore, the observed Fe^{4+} and Fe^{3+} valence states can be assigned to the Fe(1) and Fe(2) crystallographic sites, respectively. The bond-strength sum values obtained for the $Fe^{4+}O_5$ and $Fe^{3+}O_6$ polyhedra units ($\sum s = 4.09$ and 2.84, respectively) in $Sr_4Fe_4O_{11}$ are very close to the corresponding Fe^{4+} and Fe^{3+} sums obtained in other related strontium iron oxide compounds (see Table 11).

TABLE 6
Structural Parameters for $Sr_4Fe_4O_{11}$ Refined in Space Group *C*12/*m*1

Atom	Site	x	y	z	$U_{iso} \times 10^2$ (Å^2)
Sr(1)	8*j*	0.1206(5)	0.2308(4)	0.757(1)	0.3(1)
Fe(1)	4*i*	0.126(2)	0	0.247(4)	0.6(1)
Fe(2)	4*i*	0.372(2)	0	0.750(4)	0.5(2)
O(1)	8*i*	0.117(1)	0.2212(5)	0.232(2)	1.9(1)
O(2)	4*i*	0.2615(6)	0	0.008(4)	0.9(2)
O(3)	2*b*	0	1/2	0	0.7(2)
O(4)	2*d*	1/2	0	1/2	1.4(3)
O(5)	2*c*	0	0	1/2	1.2(2)
O(6)	4*i*	0.2670(5)	0	0.496(3)	0.6(1)

Note. $a = 10.974(1)$ Å, $b = 7.702(1)$ Å, $c = 5.473(1)$ Å, $\beta = 90.03(1)°$. $R_{wp} = 0.110$, $R_p = 0.066$, $R_e = 0.057$, $R_I = 0.063$, $S = 1.920$.

With regard to the $Fe(2)O_6$ octahedron in $Sr_4Fe_4O_{11}$, the observed distortion is attributed to the anisotropic

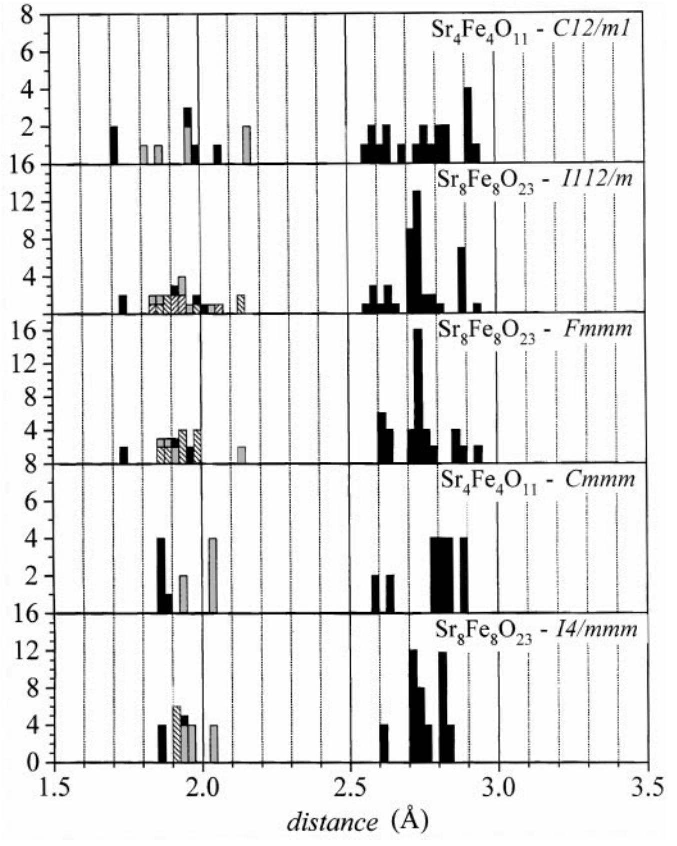

FIG. 11. Fe–O and O–O bond-length distributions for (a) $Sr_4Fe_4O_{11}$ *C*12/*m*1, (b) $Sr_8Fe_8O_{23}$ *I*112/*m*, (c) $Sr_8Fe_8O_{23}$ *Fmmm*, (d) $Sr_4Fe_4O_{11}$ *Cmmm*, and (e) $Sr_8Fe_8O_{23}$ *I*4/*mmm* structural models.

distribution of nearest-neighbor Fe^{3+} and Fe^{4+} cations, rather than a localized Jahn–Teller effect. In support of this conclusion, the $Fe^{3+}O_6$ octahedra present in $Sr_2Fe_2O_5$ are distorted to a similar degree by the local anisotropic crystal lattice.

The effects of electronic configuration on Fe–O bonding are evident when comparing $Sr_3Fe_2O_6$ and $Sr_4Fe_4O_{11}$. In $Sr_3Fe_2O_6$, the high-spin d^5 isotropic electronic configuration of the Fe^{3+} cation means that it cannot gain any directional crystal field stabilization from the O_5 square-pyramidal coordination. As such, the position of the Fe^{3+} cation along the principal axis of the FeO_5 unit will largely be determined by ionic forces, resulting in $d(\text{Fe–O}_a) < d(\text{Fe–O}_b)$ (O_a and O_b represent the axial and basal oxygen atoms). This is observed in $Sr_3Fe_2O_6$ where $d(\text{Fe–O}_a) = 1.886$ Å and $d(\text{Fe–O}_b) = 1.980$ Å (40). In contrast to this situation, in $Sr_4Fe_4O_{11}$ the Fe(1)O_5 central high-spin $Fe^{4+}:d^4$ cation is able to gain crystal field stabilization energy through the unequal occupation of the anti-bonding a^*_{1g} and b^*_{1g} orbitals (these orbitals are predominately of $d(z^2)$ and $d(x^2-y^2)$ character, respectively). The observation of $d(\text{Fe(1)–O}_a) > d(\text{Fe(1)–O}_b)$ in $Sr_4Fe_4O_{11}$ (see Table 9) supports a preferential occupation of a lower lying anti-bonding a^*_{1g} orbital. In the closely related oxygen-vacancy ordered perovskite $Ca_2Mn_2O_5$, the vacancies are ordered to yield a crystal structure composed of vertex-sharing MnO_5 square-pyramidal units (41). The central Mn^{3+} cation also possesses a high-spin d^4 configuration and a similar preferential occupation of the anti-bonding a^*_{1g} orbital affects the Mn–O bond lengths.

Semiconducting behavior, with an activation energy for conduction of $E_a = 0.053$ eV and $\sigma \approx 10^{-1}$ and 10^2 S cm^{-1} at 300 K, has been reported for $SrFeO_x$ samples with $x = 2.72$ and 2.78 (42), respectively. It is reasonable to assume that the conductivity properties of $SrFeO_x$ do not change drastically over this small composition range. To rationalize the semiconducting nature of $Sr_4Fe_4O_{11}$, which corresponds to $x = 2.75$, it is best to first consider $Sr_4Fe_4O_{11}$ in the context of the three-dimensional *p–d* charge-transfer metal $SrFeO_3$, described earlier.

In $Sr_4Fe_4O_{11}$, the contribution to conduction by $O:2p \rightarrow Fe:3d$ charge-transfer fluctuations will largely be determined by the intracluster and intercluster coupling of $(Fe^{4+}O_5)_2$ bow-tie units. Clearly, the intercluster interactions between the $(Fe^{4+}O_5)_2$ units will be greatly reduced by the lower number density and associated increased separation, relative to the $Fe^{4+}O_6$ intercluster interactions in $SrFeO_3$. Consequently, this will result in a much narrower W_p bandwidth of the d^5L^{-1} state and an opening of a bandgap between the localized $Fe:d^4$ and itinerant d^5L^{-1} states. A related bandgap opening has been reported for the system $Sr_{m+1}Fe_mO_{3m+1}$ ($m = 1, 2$, and ∞), where the number of nearest-neighbor $Fe^{4+}O_6$ units decreases as m is lowered toward the two-dimensional end member Sr_2FeO_4 ($m = 1$) (35, 43, 44). Demonstrating the trend toward more localized electronic behavior, increasing activation energies for conduction of $E_a = 0.12$ and 0.18 eV have been determined for $m = 2$ and 1 members, $(Sr_{2.7}Ba_{0.3})Fe_2O_7$ and Sr_2FeO_4, respectively (44, 45). The much lower activation energy for conduction of $E_a = 0.053$ eV found in $Sr_4Fe_4O_{11}$ cannot be accounted for by an $O:2p \rightarrow Fe:3d$ charge-transfer fluctuations mechanism alone. Differing from the $Sr_{m+1}Fe_mO_{3m+1}$ series, $Sr_4Fe_4O_{11}$ is a mixed-valence compound, and therefore one should consider nearest-neighbor charge-hopping fluctuations of the type $Fe^{4+}O_5 + Fe^{3+}O_6 \leftrightarrow Fe^{3+}O_5 + Fe^{4+}O_6$. Such fluctuations are anticipated to be of a low activation energy, since the excited states of $Fe^{3+}O_5$ and $Fe^{4+}O_6$ are easily stabilized as ground states; see, for example, the closely related compounds $Sr_3Fe_2O_6$ and $Sr_3Fe_2O_7$ (40). We therefore propose that it is these charge-hopping fluctuations that are primarily responsible for the semiconducting behavior of $Sr_4Fe_4O_{11}$ (42).

The unusual magnetic properties of $Sr_4Fe_4O_{11}$ can be related to the crystal structure and charge order of the Fe^{4+} and Fe^{3+} cations. The magnetic structure that evolves in

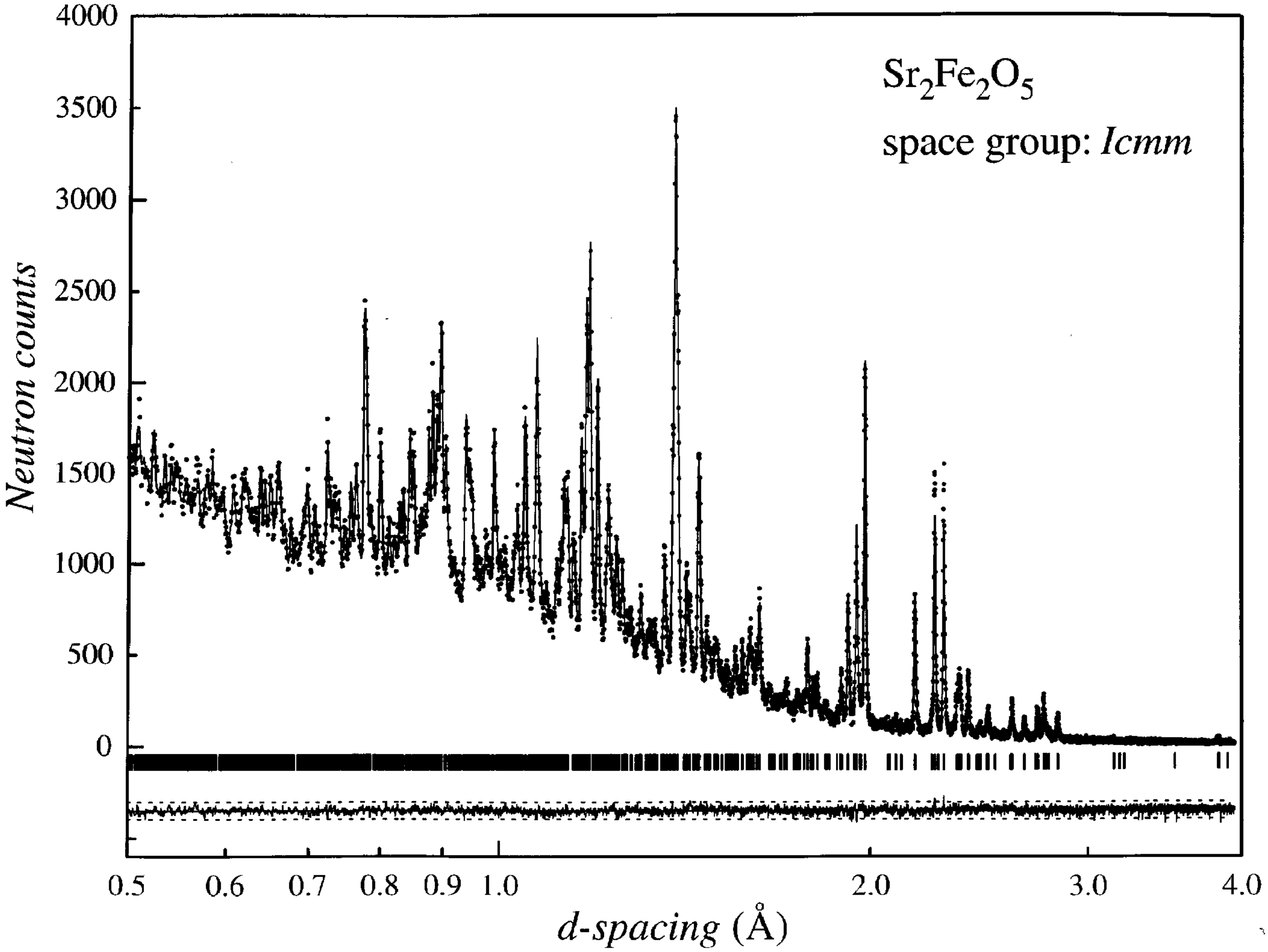

FIG. 12. Neutron powder diffraction data and Rietveld refinement profile for $Sr_2Fe_2O_5$ refined in the *Icmm* space group. Format is the same as for Fig. 4.

$Sr_4Fe_4O_{11}$ on cooling is determined largely by the superexchange interactions between the Fe cations. The observation of a hyperfine magnetic splitting and low flux density saturation value of the Fe^{3+} component, combined with only a linewidth broadening of the Fe^{4+} component, is suggestive of a partially frustrated antiferromagnet. Furthermore, a strong divergence between zero-field-cooled and field-cooled magnetic susceptibility curves was observed for $Sr_4Fe_4O_{11}$ (10). This magnetic behavior is much like that of a spin-glass transition as observed in a variety of Fe-containing perovskite-derived oxides. Examples include the magnetically dilute $SrAFeBO_6$ (A = Sr, Ca, Ba; B = Nb, Sb, Ta) (46–48) systems, where it is believed that competing nearest-neighbor and next-nearest-neighbor exchange interactions prevent the development of long-range magnetic order. More recently, a magnetically nondilute $Sr_{2.6}La_{0.4}Fe_2O_7$ frustrated antiferromagnetic material ($T_N \approx 50$ K) has been reported (44). This material is perhaps more closely related to $Sr_4Fe_4O_{11}$ since its magnetic properties are presumably determined by interactions between Fe^{3+} and Fe^{4+} cations.

One can envision a plausible magnetic structure for $Sr_4Fe_4O_{11}$ as follows. Below the Néel temperature of ~230 K, the Fe(2) sublattice of Fe^{3+} cations forms an antiferromagnet spin structure, with the coupling mediated by Fe–O–Fe superexchange interactions parallel to the y-axis direction and Fe–O–O–Fe super-superexchange interactions within ($Fe^{3+}Fe^{4+}O_4$) xz-planes. Each Fe^{4+} cation will then have two Fe^{3+} neighbors with “up” magnetic moment and two with “down”. Irrespective of whether the Fe^{3+}–O–Fe^{4+} superexchange interactions are ferro- or antiferromagnetic the Fe^{4+} magnetic moments will be topologically frustrated due to the opposite spin alignments of the nearest-neighbor Fe^{3+} cations that define a dominant antiferromagnetic lattice. Assuming Fe^{3+}–O–Fe^{4+} ferromagnetic superexchange interactions to be the most

TABLE 7
Structural Parameters for $Sr_4Fe_4O_{11}$ Refined in Space Group *Icmm*

Atom	Site	x	y	z	$U_{iso} \times 10^2$ (Å^2)
Sr	8*h*	0.0144(4)	0.1093(1)	1/2	0.8(1)
Fe(1)[a]	4*a*	0	0	0	0.4(1)
Fe(2)[b]	8*i*	0.932(1)	1/4	0.955(1)	0.2(2)
O(1)	8*g*	1/4	0.9920(2)	1/4	0.7(1)
O(2)	8*h*	0.0503(4)	0.1406(2)	0	1.2(1)
O(3)	8*i*	0.860(1)	1/4	0.625(1)	0.8(1)

Note. $a = 5.672(1)$ Å, $b = 15.59(2)$ Å, $c = 5.527(1)$ Å.
$R_{wp} = 0.082$, $R_p = 0.054$, $R_e = 0.050$, $R_I = 0.051$, $S = 1.652$.
[a] Magnetic moment $\mu_z = 3.85(7)\ \mu_B$.
[b] Magnetic moment $\mu_z = -3.67(8)\ \mu_B$.
The 8*i* sites are only half occupied.

probable, a schematic representation of this magnetic model highlighting the proposed exchange interactions within an ($Fe^{3+}Fe^{4+}O_4$) xz-plane is shown in Fig. 13. Strong antiferromagnetic superexchange interactions, parallel to the y-axis direction, are expected between adjacent ($Fe^{3+}Fe^{4+}O_4$) planes. However, these do not relieve the topological frustration. At present it is unknown whether the magnetic Fe^{4+} sublattice forms a spin-glass structure at or below $T_{N_2} \approx 230$ K, or if the Fe^{4+} sublattice remains paramagnetic and possibly undergoes a separate spin-ordering transition at very low temperatures, $T_{N_2} < 4.2$ K. This proposed magnetic model for $Sr_4Fe_4O_{11}$ is fairly simple and neglects the effects of electron-hopping processes, possible canting of the Fe^{3+} magnetic moments, and $O^{2-}:2p \rightarrow Fe^{4+}:3d$ charge transfer. A related magnetic structure has previously been reported for RNiO$_3$ (R = Nd, Sm) (49, 50). In these RNiO$_3$ compounds, the dominate Ni^{3+} antiferromagnetic spin structure results in two inequivalent R^{3+} sublattices. One R^{3+} sublattice is antiferromagnetically ordered while the other R^{3+} sublattice experiences a null polarization field and remains paramagnetic.

TABLE 8
Mössbauer Parameters at ~300 K for the Oxygen-Vacancy-Ordered Perovskite $Sr_nFe_nO_{3n-1}$ Series

Compound	Component	δ (mm s^{-1})	Int. (%)	Ref.
$Sr_2Fe_2O_5$	Fe^{3+} (*O*)	0.37	50	30
	Fe^{3+} (*T*)	0.19	50	
$Sr_4Fe_4O_{11}$	Fe^{3+}	0.35	50	28
	Fe^{4+}	-0.08	50	
$Sr_8Fe_8O_{23}$[a]	$Fe^{3.5+}$	0.17	50	12
	Fe^{4+}	0.04	50	
$SrFeO_3$	Fe^{4+}	0.08	100	37

[a] The measured $Fe^{3.5+}$ and Fe^{4+} component intensities were 55 and 45% respectively, for a sample of composition $SrFeO_{2.86}$. For $Sr_8Fe_8O_{23}$ ($SrFeO_{2.875}$) equal component intensities of 50% can be assumed.

TABLE 9
Interatomic Distances (Å) and Bond Angles (°) for the *Cmmm* Crystal Structure of $Sr_4Fe_4O_{11}$

Sr(1)–O(1)	2.736(1)	×2
Sr(1)–O(2)	2.530(4)	×2
Sr(1)–O(3)	2.887(2)	×8
Sr(2)–O(2)	2.957(4)	×2
Sr(2)–O(3)	2.605(2)	×8
Sr(3)–O(1)	2.647(3)	×1×2
Sr(3)–O(2)	2.739(1)	×2×2
Sr(3)–O(3)	2.823(3)	×8×2
	Square-pyramidal Fe(1) site ×2	
Fe(1)–O(1)	1.90(1)	×1
Fe(1)–O(3)	1.855(2)	×4
O(1)–Fe(1)–O(3)	97.0(3)	×4
O(3)–Fe(1)–O(3)	90.1(2)	×2
O(3)–Fe(1)–O(3)	88.2(2)	×2
O(3)–Fe(1)–O(3)	166.0(5)	×2
O(1)–O(3)	2.813(2)	×4
O(3)–O(3)	2.625(5)	×2
O(3)–O(3)	2.582(5)	×2
	Octahedral Fe(2) site ×2	
Fe(2)–O(2)	1.937(1)	×2
Fe(2)–O(3)	2.044(2)	×4
O(2)–Fe(2)–O(3)	91.2(1)	×4
O(2)–Fe(2)–O(3)	88.8(1)	×4
O(3)–Fe(2)–O(3)	90.0(2)	×4
O(2)–O(3)	2.845(2)	×4
O(2)–O(3)	2.787(3)	×4
O(3)–O(3)	2.890(5)	×4

The low internal flux density, $B_{hf} = 46$ T (13, 28), observed for the Fe^{3+} component in $Sr_4Fe_4O_{11}$ can be compared with the flux densities of $B_{hf} = 56$, 54, and 50 T, measured for $Fe^{3+}O_6$ octahedra in $LaFeO_3$, $Sr_2Fe_2O_5$, and $SrLaFeO_4$, respectively (28, 30, 51). In $LaFeO_3$ and $Sr_2Fe_2O_5$ strong antiferromagnetic coupling occurs in all three dimensions, whereas in $LaSrFeO_4$, because of intervening ($La_{0.5}Sr_{0.5}$)O layers, strong superexchange interactions are limited to two dimensions and consequently there is a ~4 T reduction in the measured saturation field. In $Sr_4Fe_4O_{11}$, the low $B_{hf} = 46$ T saturation flux density, a reduction therefore of ~8 T, is suggestive of strong superexchange interactions occurring in only one dimension. This is

TABLE 10
Bond-Strength Sums Calculated for Fe Cations in $Sr_4Fe_4O_{11}$ (See Text for Details of Calculations)

Site	Coordination	Fe^{3+}[a]	Fe^{4+}[b]
Fe(1)	Square pyramid	3.17	4.09
Fe(2)	Octahedron	2.84	3.57

[a] Absolute ionic radius $\rho_0 = 0.621$ Å.
[b] Absolute ionic radius $\rho_0 = 0.660$ Å.

TABLE 11
Bond-Strength Sums Calculated for Fe Cations in Related Sr–Fe–O Compounds

Compound	Site cation	Coordination	$\sum s$	Ref.
$Sr_2Fe_2O_5$	Fe^{3+}	Octahedron	2.66	This work
	Fe^{3+}	Tetrahedron	2.52	This work
$Sr_3Fe_2O_6$	Fe^{3+}	Square pyramid	2.58	40
$SrFeO_3$	Fe^{4+}	Octahedron	4.21	This work
$Sr_3Fe_2O_7$	Fe^{4+}	Octahedron	4.13	40
Sr_2FeO_4	Fe^{4+}	Octahedron	4.09	53

consistent with the determined crystal structure of $Sr_4Fe_4O_{11}$ where one-dimensional chains of vertex-linked $Fe^{3+}O_6$ octahedra are separated from one another by $Fe^{4+}O_5$ square pyramids (see Fig. 10a).

$Sr_8Fe_8O_{23}$

The room-temperature Mössbauer spectrum of $Sr_8Fe_8O_{23}$ consists of two components of equal intensity. The first component, with an isomer shift of $\delta = 0.04\ \mathrm{mm\,s^{-1}}$, can be readily assigned to Fe^{4+} cations. The second component, which cannot be attributed to the presence of charge-compensating Fe^{3+} cations, possesses an isomer shift of $\delta = 0.17\ \mathrm{mm\,s^{-1}}$ which is intermediate in value for Fe^{4+} and Fe^{3+} valence states. The second component is therefore assigned to nominally average-valence $Fe^{3.5+}$ cations. On cooling $Sr_8Fe_8O_{23}$, substantial linewidth broadening of the two Mössbauer components occurs on approaching ~85 K and below this temperature a magnetic hyperfine pattern evolves. At 4 K the Mössbauer spectrum consists of components arising from Fe^{3+} and Fe^{4+} cations, presumably in a 1:3 intensity ratio; however, their relative intensities have not been accurately determined. High-spin configurations for the Fe^{3+} and Fe^{4+} cations are signified by the observed flux densities of $B_{hf} = 44$ and 29 T, respectively. It appears that an ordering of Fe^{4+} and Fe^{3+} cations, or, at minimum, a slowing of the intervalence charge-transfer processes to $\tau \geq 10^{-8}$ s, thereby splitting the $Fe^{3.5+}$ component has occurred (13).

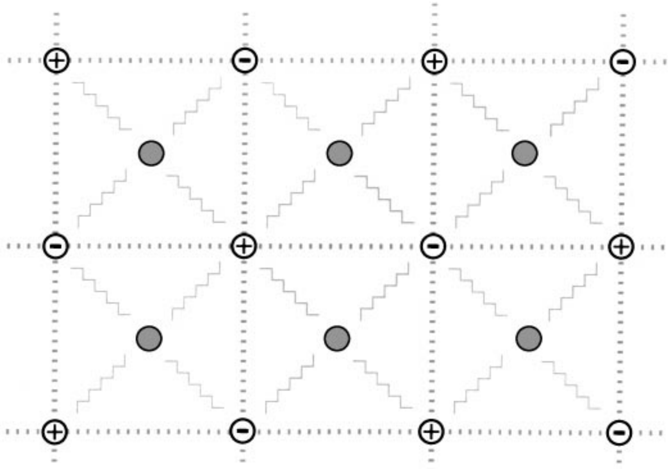

FIG. 13. Schematic representation of the proposed geometrically frustrated magnetic model for $Sr_4Fe_4O_{11}$. Antiferromagnetic and frustrated-ferromagnetic exchange paths are represented by the dash and zig-zag lines, respectively. "Up" and "down" spin-direction Fe^{3+} magnetic sites are indicated by the + and − symbols, and the gray filled circles represent the Fe^{4+} sites.

The room-temperature crystal structure of $Sr_8Fe_8O_{23}$ contains three crystallographically distinct Fe sites in a 1:2:1 abundance (Fe(1):Fe(2):Fe(3), respectively). The Fe(1) site has a square-pyramidal oxygen coordination, whereas both the Fe(2) and Fe(3) sites have octahedral coordination. To assign the observed room-temperature valence states of $Fe^{3.5+}$ and Fe^{4+} to their corresponding crystallographic Fe sites, Fe–O bond-strength sums were calculated around each of the Fe sites. The results are presented in Table 13. An examination of Table 13 clearly indicates that the Fe(2) cation possesses a lower valence than either the Fe(1) or Fe(3) cation. The average valence $Fe^{3.5+}$ state can, therefore, be assigned to the Fe(2) cation, with the remaining Fe(1) and Fe(3) cations being in the Fe^{4+} valence state.

In support of these assignments, the $Fe(1)O_5$ and $Fe(3)O_6$ polyhedra are almost identical, with regard to internal bond lengths and bond angles (see Table 12), to comparable $Fe^{4+}O_k$ polyhedra present in $Sr_4Fe_4O_{11}$ (see Table 10) and $SrFeO_3$ (d(Fe–O) = 1.926(1) Å). Again, $d(\mathrm{Fe{-}O_a}) > d(\mathrm{Fe{-}O_b})$ is observed for the FeO_5 unit, consistent with the assigned $Fe^{4+}:d^4$ valence state and a preferential occupation of an antibonding a_{1g}^* orbital.

For the $Fe(2)O_6$ octahedra, an average $Fe^{3.5+}$ valence state associated with the formation of a metallic σ^* band across the Fe(2) cation sites can effectively be dismissed because such a band would certainly encompass the Fe(1) and Fe(3) sites and, consequently, a single $Fe^{3.75+}$ average-valence state would result. The observed $Fe^{3.5+}$ valence state is, therefore, concluded to result from fast-electron-transfer processes between high-spin $Fe^{4+}:d^4$ and $Fe^{3+}:d^5$ cations. Obviously, such charge-hopping processes will affect the electronic conductivity of $Sr_8Fe_8O_{23}$. Similar to $Sr_4Fe_4O_{11}$, semiconducting behavior with an activation energy for conduction of $E_a \approx 0.02$ eV and $\sigma \approx 10^3\ \mathrm{S\,cm^{-1}}$ at 300 K has been reported for $SrFeO_x$ samples near $Sr_8Fe_8O_{23}$ (42, 52). Differing from the electronic situation in $Sr_4Fe_4O_{11}$, the intercluster coupling between $Fe^{4+}O_k$ (k = 5 and 6) units is expected to be significantly stronger, and, consequently, a much smaller bandgap between localized $Fe{:}d^4$ and itinerant d^5L^{-1} states is predicted for $Sr_8Fe_8O_{23}$. Considering these factors, it appears likely that the nearly metallic conductivity of $Sr_8Fe_8O_{23}$ is the result of

TABLE 12
Interatomic Distances (Å) and Bond Angles (°) for the *I*4/*mmm* Crystal Structure of $Sr_8Fe_8O_{23}$

Sr(1)–O(2)	2.631(3)	×4×2
Sr(1)–O(3)	2.842(3)	×2×2
Sr(1)–O(4)	2.685(2)	×4×2
Sr(1)–O(5)	2.648(3)	×1×2
Sr(2)–O(1)	2.742(4)	×1×2
Sr(2)–O(2)	2.887(3)	×4×2
Sr(2)–O(3)	2.625(3)	×2×2
Sr(2)–O(4)	2.722(2)	×4×2
Sr(2)–O(5)	2.722(4)	×1×2
	Square-pyramidal Fe(1) site	
Fe(1)–O(1)	1.926(1)	×1
Fe(1)–O(2)	1.851(4)	×4
O(1)–Fe(1)–O(2)	96.5(4)	×4
O(2)–Fe(1)–O(2)	89.3(1)	×4
O(2)–Fe(1)–O(2)	166.9(7)	×2
O(1)–O(2)	2.820(3)	×4
O(2)–O(2)	2.601(4)	×4
	Octahedral Fe(2) site ×2	
Fe(2)–O(2)	2.036(3)	×2
Fe(2)–O(3)	1.931(1)	×2
Fe(2)–O(4)	1.952(3)	×2
O(2)–Fe(2)–O(3)	91.4(2)	×2
O(2)–Fe(2)–O(3)	88.4(2)	×2
O(2)–Fe(2)–O(4)	90	×4
O(3)–Fe(2)–O(4)	90	×4
O(2)–Fe(2)–O(2)	180	×1
O(3)–Fe(2)–O(3)	180	×1
O(4)–Fe(2)–O(4)	180	×1
O(2)–O(3)	2.839(4)	×2
O(2)–O(3)	2.772(5)	×2
O(2)–O(4)	2.820(3)	×4
O(3)–O(4)	2.745(2)	×4
	Octahedral Fe(3) site	
Fe(3)–O(4)	1.912(3)	×4
Fe(3)–O(5)	1.925(1)	×2
O(4)–Fe(3)–O(4)	90	×4
O(4)–Fe(3)–O(5)	90	×8
O(4)–O(4)	2.704(4)	×4
O(4)–O(5)	2.713(2)	×8

TABLE 13
Bond-Strength Sums Calculated for Fe Cations in $Sr_8Fe_8O_{23}$ (See Text for Details of Calculations)

Site	Coordination	No.	Fe^{3+}	Fe^{4+}	$Fe^{3.5+}$[a]	$Fe^{3.5+}$[b]
Fe(1)	Square pyramid	1	3.16	4.08	3.62	3.63
Fe(2)	Octahedron	2	3.03	3.83	3.43	3.45
Fe(3)	Octahedron	1	3.37	4.30	3.84	3.85

[a] Average of Fe^{3+} and Fe^{4+} bond-strength sums.

[b] Calculated using an average absolute ionic radius, $\rho_0 = 0.641$ Å, of the Fe^{3+} and Fe^{4+} values.

both $O:2p \rightarrow Fe:3d$ charge transfer and $Fe^{4+}O_6 + Fe^{3+}O_6 \leftrightarrow Fe^{3+}O_6 + Fe^{4+}O_6$ charge-hopping fluctuations.

Interestingly, the $Fe(3)O_6$ octahedron, in being almost regular, $d(Fe\text{–}O_a)/d(Fe\text{–}O_e) = 1.006$ (where O_e refers to equatorial oxygen atoms), displays no evidence of a localized static Jahn–Teller effect that one would normally expect of an $Fe^{4+}:d^4$ cation. Since $Sr_8Fe_8O_{23}$ is a semiconductor the absence of a Jahn–Teller distortion cannot be attributed to the formation of a delocalized e_g^* band, as has previously been asserted for explaining the Jahn–Teller effect's absence in the metal $SrFeO_3$ (29). In the related compounds $Sr_3Fe_2O_7$ and Sr_2FeO_4, which are both semiconducting and contain, formally, only high-spin $Fe^{4+}:d^4$ cations (44, 45), the FeO_6 octahedra units are also nearly regular, $d(Fe\text{–}O_a)/d(Fe\text{–}O_e) = 1.010$ and 1.009 (40, 53). The absence of any Jahn–Teller effect (static or dynamic) in $SrFeO_3$, $Sr_8Fe_8O_{23}$, $Sr_3Fe_2O_7$, and Sr_2FeO_4, can, therefore, be attributed to the large weight of the charge-transfer d^5L^{-1} state in the mixed $\Psi_g(^5E_g) = a|d^4, {}^5E_g\rangle + b|d^5L^{-1}, {}^5E_g\rangle$ ground state of the formally Fe^{4+} cations (6).

It is expected that the ground-state weight of the d^5L^{-1} configuration (b in the above formula) increases from the more isolated Fe^{4+} cations found in $LaSr(Li_{0.5}Fe_{0.5})O_4$ (54) via the two-dimensional Sr_2FeO_4 to the three-dimensional $SrFeO_3$. In accordance with the increasing shielding of s electron density from the Fe nucleus, more positive Mössbauer isomer shift values, $\delta = -0.18$, -0.02, and 0.08 mm s^{-1} respectively, are observed along this series. In the vacancy-ordered perovskite $Sr_nFe_nO_{3n-1}$ series, a similar dependence is observed. The Fe^{4+} state isomer shift value increases, $\delta = -0.08$, 0.04, and 0.08 mm s^{-1}, from $Sr_4Fe_4O_{11}$ via $Sr_8Fe_8O_{11}$ to $SrFeO_3$, respectively (see Table 8). At present it is not known the degree to which this effect, in the $Sr_nFe_nO_{3n-1}$ series, is associated with the increasing intercluster coupling of the $Fe^{4+}O_k$ units, as opposed to the intracluster increasing average oxygen coordination of the $Fe^{4+}O_k$ units ($k = 5$, 5.5, and 6 for $n = 4$, 8, and 8).

CONCLUSIONS

This work on the $Sr_nFe_nO_{3n-1}$ ($n = 2$, 4, 8, and ∞) system illustrates the care that must be exercised in determining correct crystal structures of oxygen-vacancy-ordered compounds. It also shows that, when correct structures are determined, one can achieve consistent assignments of Fe cation valence states and agreement with local-probe data, such as Mössbauer. An accurate knowledge of the respective crystal structures and valence states of the crystallographically distinct Fe sites has proved invaluable for rationalizing trends in the electronic and magnetic properties across the $Sr_nFe_nO_{3n-1}$ series.

A simple cubic perovskite crystal structure has been confirmed for the end-member compound $SrFeO_3$ ($n = \infty$). For this compound, no structural evidence was found signifying a static or dynamic Jahn–Teller effect, associated with the formally $Fe^{4+}:d^4$ cations. The absence of a Jahn–Teller effect was attributed to a large weight of the charge-transfer d^5L^{-1} state in the mixed $\Psi_g(^5E_g) = a|d^4, {}^5E_g\rangle + b|d^5L^{-1}, {}^5E_g\rangle$, ground-state configuration.

In the case of the opposite end member, $Sr_2Fe_2O_5$ ($n = 2$), a disordered brownmillerite-type nuclear and G-type antiferromagnetic spin structure was concluded from a comparison of Rietveld refinements of ordered and disordered models. Additional support for the disordered structure of $Sr_2Fe_2O_5$ was indirectly provided by the low refined values of the Fe^{3+} magnetic moments. These low magnetic moments were attributed to the presence of structural disorder and the resulting imperfect alignment of magnetic spins.

For the mixed-valence $Sr_4Fe_4O_{11}$ ($n = 4$) and $Sr_8Fe_8O_{23}$ ($n = 8$) compounds, we have shown that all previously proposed structural models are incorrect. The correct crystal structures were concluded by comparison of Rietveld refinements for several closely related structural models. The differences observed in these refinements were statistically significant, but subtle. The reason for this is that the correct and incorrect crystal structures of $Sr_4Fe_4O_{11}$ and $Sr_8Fe_8O_{23}$ differed essentially from one another only by the orientation of the oxygen-vacancy sublattice with respect to the underlying perovskite crystal structure. Of note, the refinements using incorrect models (Figs. 6, 7, and 9) actually look quite good. Many refinements of equivalent quality are in the published literature and are accepted as being correct. This observation emphasizes the importance of testing all possible models in such studies and of employing additional tests of the validity of the structure, where possible. In the present work, comparisons of the bond-length distributions for the correct and incorrect models provided an important confirmation of the Rietveld refinements.

The correct crystal structures of $Sr_4Fe_4O_{11}$ and $Sr_8Fe_8O_{23}$ having been established, assignments of specific valence states to their respective crystallographic Fe cation sites (consistent with published Mössbauer data) were achieved through the use of bond-strength sums. For $Sr_4Fe_4O_{11}$ which has a crystal structure composed of vertex-sharing $Fe(1)O_5$ square pyramids and $Fe(2)O_6$ octahedra (see Fig. 10a), Fe^{3+} and Fe^{4+} cations were found to occupy the Fe(1) and Fe(2) sites, respectively. Considering the expected magnetic superexchange interactions resulting from this crystallographic ordering of Fe^{3+} and Fe^{4+} cations, we have proposed, for $Sr_4Fe_4O_{11}$, a unique magnetic structure. In this model, at temperatures below $T_N \approx 230$ K, the Fe(2) sublattice forms a dominant antiferromagnetic spin structure, while conversely, the Fe(1) magnetic spins being subject to conflicting ferromagnetic superexchange interactions do not order cooperatively. The Fe(1) spins either remain paramagnetic or form a spin-glass structure.

ACKNOWLEDGMENTS

This work was supported by ARPA/ONR, DOE-BES Contract No. W-31-109-ENG-38, and the State of Illinois under HECA.

REFERENCES

1. P. K. Gallagher, J. B. MacChesney, and D. N. E. Buchanan, *J. Chem. Phys.* **41,** 2429 (1964).
2. J. B. MacChesney, R. C. Sherwood, and J. F. Potter, *J. Chem. Phys.* **43,** 1907 (1965).
3. T. Takeda and H. Watanabe, *J. Phys. Soc. Jpn.* **33,** 973 (1972).
4. T. Takeda, Y. Yamaguchi, and H. Watanabe, *J. Phys. Soc. Jpn.* **33,** 967 (1972).
5. H. Adachi and M. Takano, *J. Solid State Chem.* **93,** 556 (1991).
6. A. E. Bouquet, A. Fujimori, T. Mizokawa, T. Saitoh, H. Nagatame, S. Suga, N. Kimizuki, Y. Takeda, and M. Takano, *Phys. Rev. B* **45,** 1561 (1992).
7. M. Abbate, F. M. F. de Groot, J. C. Fuggle, A. Fujimori, Q. Strebel, F. Lopez, M. Domke, G. Kaindl, G. A. Sawatzky, M. Takano, and Y. Takeda, *Phys. Rev. B* **45,** 1561 (1992).
8. M. Takano, J. Kawachi, N. Nakanishi, and Y. Takeda, *J. Solid State Chem.* **39,** 75 (1981).
9. B. C. Tofield, C. Greaves, and B. E. F. Fender, *Mater. Res. Bull.* **10,** 737 (1975).
10. T. C. Gibb, *J. Chem. Soc., Dalton Trans.* 1455 (1985).
11. J.-C. Grenier, N. Ea, M. Pouchard, and P. Hagenmuller, *J. Solid State Chem.* **58,** 243 (1985).
12. Y. Takeda, K. Kanno, T. Takeda, O. Yamamoto, M. Takano, N. Nakayama, and Y. Bando, *J. Solid State Chem.* **63,** 237 (1986).
13. M. Takano, T. Okita, N. Nakayama, Y. Bando, Y. Takeda, O. Yamamoto, and J. B. Goodenough, *J. Solid State Chem.* **73,** 140 (1988).
14. W. Sturhahn, T. S. Toellner, E. E. Alp, X. Zhang, M. Ando, Y. Yoda, S. Kikuta, M. Seto, C. W. Kimball, and B. Dabrowski, *Phys. Rev. Lett.* **74,** 3832 (1995).
15. J. D. Jorgensen, J. J. Faber, J. M. Carpenter, R. K. Crawford, J. R. Haumann, R. L. Hittermann, R. Kleb, G. E. Ostrowski, F. J. Rotella, and T. G. Worton, *J. Appl. Crystallogr.* **22,** 321 (1989).
16. H. M. Rietveld, *J. Appl. Crystallogr.* **2,** 65 (1969).
17. A. C. Larson and R. B. von-Dreele, "General Structure Analysis System", Los Alamos National Laboratories, Report LAUR 86-748, LANL, Los Alamos, NM, 1986–1997.
18. P. J. Brown, Magnetic scattering of neutrons, *in* "International Tables for Crystallography" (A. J. C. Wilson, Ed.), Vol. C, Kluwer, Dordrecht, 1992.
19. A. A. Colville, *Acta Crystallogr. B.* **26,** 1469 (1970).
20. A. A. Colville and S. Geller, *Acta Crystallogr. B* **27,** 2311 (1971).
21. C. Greaves, A. J. Jacobson, B. C. Tofield, and B. E. F. Fender, *Acta Crystallogr. B* **31,** 641 (1975)
22. M. Von-Harder and J. K. Müller-Bucshbaum, *Z. Anorg. Allg. Chem.* **464,** 169 (1980).
23. P. D. Battle, T. C. Gibb, and P. Lightfoot, *J. Solid State Chem.* **76,** 334 (1988).
24. T. Takeda, Y. Yamaguchi, and H. Watanabe, *J. Phys. Soc. Jpn* **33,** 970 (1972).
25. R. W. Grant, S. Geller, H. Wiedersich, U. Gonser, and L. D. Fullmer, *J. Appl. Phys.* **39,** 1122 (1968)
26. Z. Friedman, H. Shaked, and S. Shtrikman, *Phys. Letters* **25A,** 9 (1967)

27. T. Takeda, Y. Yamaguchi, S. Tomiyoshi, M. Fukase, M. Sugimoto, and H. Watanabe, *J. Phys. Soc. Jpn* **24,** 446 (1968).
28. T. C. Gibb, *J. Mater. Chem.* **4**(9), 1445 (1994).
29. M. Takano, N. Nakanishi, Y. Takeda, S. Naka, and T. Takada, *Mater. Res. Bull.* **12,** 923 (1977).
30. P. D. Battle, T. C. Gibb, and S. Nixon, *J. Solid State Chem.* **79,** 75 (1989).
31. J. Zaanen, G. A. Sawatzky, and J. W. Allen, *Phys. Rev. Lett.* **55,** 418 (1985).
32. A. Fujimori, *J. Phys. Chem. Solids* **53,** 1595 (1992).
33. A. E. Bouquet, T. Mizokawa, T. Saitoh, H. Nagatame, and A. Fujimori, *Phys. Rev. B* **46,** 3771 (1992).
34. A. E. Bouquet, T. Saitoh, T. Mizokawa, and A. Fujimori, *Solid State Commun.* **83,** 11 (1992).
35. P. Adler, A. F. Goncharov, and K. Syassen, *Hyp. Int.* **95,** 71 (1995).
36. L. Fournés, Y. Potin, J.-C. Grenier, G. Damazeau, and M. Pouchard, *Solid State Commun.* **62,** 239 (1987).
37. A. Wattiaux, L. Fournés, A. Demourgues, N. Bernben, J.-C. Grenier, and M. Pouchard, *Solid State Commun.* **77,** 489 (1991).
38. J. A. M. Van Roosmalen and E. H. P. Cordfunke, *J. Solid State Chem.* **93,** 212 (1991).
39. J. Ziólkowski, *J. Solid State Chem.* **57,** 269 (1985).
40. S. E. Dann, M. T. Weller, and D. B. Currie, *J. Solid State Chem.* **97,** 179 (1992).
41. K. R. Poeppelmeier, M. E. Leonowicz, J. C. Scanlon, J. M. Longo, and W. B. Yelon, *J. Solid State Chem.* **45,** 71 (1982).
42. S. Nakamura and S. Iida, *Jpn. J. Appl. Phys.* **34,** L291 (1995).
43. P. Adler, A. F. Goncharov, K. Syassen, and E. Schönherr, *Phys. Rev. B* **50,** 11396 (1994).
44. P. Adler, *J. Solid State Chem.* **130,** 129 (1997).
45. P. Adler, *J. Solid State Chem.* **108,** 275 (1994).
46. R. Rodríguez, A. Fernandez, A. Isalgue, J. Rodríguez, A. Labarta, J. Tejada, and X. Obradors, *J. Phys. C* **18,** L401 (1985).
47. P. D. Battle, T. C. Gibb, A. J. Herod, and J. P. Hodges, *J. Mater. Chem.* **5,** 75 (1995).
48. P. D. Battle, T. C. Gibb, A. J. Herod, S. H. Kim, and P. H. Munns, *J. Mater. Chem.* **5,** 865 (1995).
49. J. L. García-Muñoz, J. Rodríguez-Caravajal, and P. Lacorre, *Phys. Rev. B* **50,** 978 (1994).
50. J. Rodríguez-Caravajal, S. Rosenkranz, M. Medarde, P. Lacorre, M. T. Fernandez-Díaz, F. Fauth, and V. Trounov, *Phys. Rev. B* **57,** 456 (1998).
51. M. Eibschutz, S. Shtrikman, and D. Treves, *Phys. Rev.* **156,** 562 (1967).
52. J. Hombo, Y. Matsumoto, and T. Kawano, *J. Solid State Chem.* **84,** 138 (1990).
53. S. E. Dann, M. T. Weller, and D. B. Currie, *J. Solid State Chem.* **92,** 237 (1991).
54. G. Demazeau, N. Chevrea, L. Fournes, J.-L. Soubeyroux, Y. Takeda, M. Thomas, and M. Pouchard, *Rev. Chim. Miner.* **20,** 155 (1983).